

Durham Research Online

Deposited in DRO:

17 March 2017

Version of attached file:

Published Version

Peer-review status of attached file:

Peer-reviewed

Citation for published item:

Ramraj, R. and Gilbank, D.G. and Blyth, S.-L. and Skelton, R.E. and Glazebrook, K and Bower, R.G. and Balogh, M.L. (2017) 'HST H grism spectroscopy of ROLES : a flatter low-mass slope for the $z \sim 1$ SSFR-mass relation.', *Monthly notices of the Royal Astronomical Society.*, 466 (3). pp. 3143-3160.

Further information on publisher's website:

<https://doi.org/10.1093/mnras/stw3262>

Publisher's copyright statement:

This article has been published in *Monthly Notices of the Royal Astronomical Society* ©: 2016 The Authors Published by Oxford University Press on behalf of the Royal Astronomical Society. All rights reserved.

Additional information:

Use policy

The full-text may be used and/or reproduced, and given to third parties in any format or medium, without prior permission or charge, for personal research or study, educational, or not-for-profit purposes provided that:

- a full bibliographic reference is made to the original source
- a [link](#) is made to the metadata record in DRO
- the full-text is not changed in any way

The full-text must not be sold in any format or medium without the formal permission of the copyright holders.

Please consult the [full DRO policy](#) for further details.

HST H α grism spectroscopy of ROLES: a flatter low-mass slope for the $z \sim 1$ SSFR–mass relation

Riona Ramraj,^{1,2} David G. Gilbank,^{1★} Sarah-Louise Blyth,² Rosalind E. Skelton,¹ Karl Glazebrook,³ Richard G. Bower⁴ and Michael L. Balogh⁵

¹South African Astronomical Observatory, PO Box 9, Observatory, 7935 Cape Town, South Africa

²Department of Astronomy, University of Cape Town, Private Bag X3, Rondebosch 7701, South Africa

³Centre for Astrophysics and Supercomputing, Swinburne University of Technology, PO Box 218, Hawthorn, VIC 3122, Australia

⁴Institute for Computational Cosmology, Department of Physics, University of Durham, South Road, Durham DH1 3LE, UK

⁵Department of Physics and Astronomy, University of Waterloo, Waterloo, ON N2L 3G1, Canada

Accepted 2016 December 13. Received 2016 December 9; in original form 2016 June 2

ABSTRACT

We present measurements of star formation rates (SFRs) for dwarf galaxies ($M_* \sim 10^{8.5} M_\odot$) at $z \sim 1$ using near-infrared slitless spectroscopy from the *Hubble Space Telescope* (*HST*) by targeting and measuring the luminosity of the H α emission line. Our sample is derived from the Redshift One LDSS3 Emission Line Survey (ROLES), which used [O II] $_{\lambda 3727}$ as a tracer of star formation to target very low stellar masses down to very low SFRs ($\sim 0.1 M_\odot \text{ yr}^{-1}$) at this epoch. Dust corrections are estimated using SED fits and we find, by comparison with other studies using Balmer decrement dust corrections, that we require a smaller ratio between the gas phase and stellar extinction than the nominal Calzetti relation, in agreement with recent findings by other studies. By stacking the Wide-Field Camera (WFC)3 spectra at the redshifts obtained from ground-based [O II] detections, we are able to push the WFC3 spectra to much lower SFRs and obtain the most complete spectroscopic measurement of the low-mass end of the SSFR–mass relation to date. We measure a flatter low-mass power-law slope (-0.47 ± 0.04) than found by other (shallower) H α -selected samples (≈ -1), although still somewhat steeper than that predicted by the Evolution and Assembly of GaLaxies and their Environments (EAGLE) simulation (-0.14 ± 0.05), hinting at possible missing physics not modelled by EAGLE or remaining incompleteness for our H α data.

Key words: galaxies: dwarf – galaxies: evolution – galaxies: general.

1 INTRODUCTION

There have been many surveys studying the star formation properties of statistical samples of galaxies out to high redshifts (e.g. Lilly et al. 1996; Madau et al. 1996; Hopkins & Beacom 2006; Karim et al. 2011; Cucciati et al. 2012). However, most of these surveys are biased towards the most massive or most actively star-forming galaxies. In order to better understand how galaxies form and evolve, we also need to study the low-mass (dwarf) galaxies. Dwarf galaxies are more numerous than their higher mass counterparts and are considered the building blocks of high-mass galaxies in the hierarchical formation scenario (e.g. White & Rees 1978; White & Frenk 1991; Springel, Frenk & White 2006).

Studies have shown that the cosmic star formation rate (SFR) has declined by an order of magnitude since $z \sim 1$, when the Uni-

verse was approximately half its current age (e.g. Hopkins & Beacom 2006). This period represents the end of the peak of SFR activity in the Universe (Madau & Dickinson 2014), which is frequently dubbed ‘Cosmic Noon’. By studying galaxies at this epoch and combining with studies at the present epoch, we can determine how galaxies have evolved over this time (i.e. the processes that have caused star formation to decline) and use this to constrain galaxy formation models (e.g. Bower, Benson & Crain 2012; Henriques et al. 2013).

The galaxy population can be divided broadly into red quiescent early-type galaxies and blue star-forming late-type galaxies (e.g. Baldry et al. 2004; Balogh et al. 2004). The physical processes governing the transition from the blue cloud to the red sequence are not yet well understood. One key discovery of recent years is the tight sequence correlating stellar mass and SFR for star-forming galaxies (Baldry et al. 2004; Noeske et al. 2007; Gilbank et al. 2010b; Whitaker et al. 2014), usually referred to as the ‘main sequence’ or ‘star-forming sequence’. This main sequence is seen

★ E-mail: gilbank@sao.ac.za

out to $z \sim 1$ (e.g. Willmer et al. 2006; Noeske et al. 2007) and even $z \sim 2$ (e.g. Brammer et al. 2009). The remarkable constancy of shape and smooth evolution of this relation argues for relatively smooth star formation histories of star-forming galaxies. In conjunction with the relatively rapid growth of passive galaxies, this hints at a smooth replenishment of star-forming galaxies as they are ‘quenched’ (Faber et al. 2007). Of particular importance is the pushing of measurements to lower stellar masses to enable any curvature of the main sequence to be measured (e.g. Whitaker et al. 2012) as this, combined with the evolution of the stellar mass function, is an important consistency check of our measurements and of galaxy evolution models (Leja et al. 2015). One of the vital ingredients that must be tested is the SFR indicator being used, which can vary between surveys and between redshifts within the same survey.

SFR indicators such as $H\alpha$ and the UV emission essentially measure the ionizing flux from young, hot massive stars, while the mid- or far-infrared emission measures the amount of the ionizing flux absorbed and re-radiated by dust. Most of the flux emitted by these young stars is at UV wavelengths. Measuring the ionizing flux from nebular emission lines (e.g. $H\alpha$ recombination line and, indirectly, the $[O\text{II}]$ forbidden line) in a galaxy’s spectrum is one way of estimating the SFR of a galaxy. In order to study evolution, one would ideally like to measure the SFR using a single indicator that can be applied from low-to-high redshifts. In practice, this is difficult because each indicator is subject to different biases and selection effects. However, $H\alpha$ is considered the most direct indicator because it traces the current star formation in a galaxy and is less affected by dust (e.g. Kennicutt 1998; hereafter K98) than shorter wavelength emission lines (such as $[O\text{II}]$) and has a small dependence on metallicity (Charlot & Longhetti 2001).

At $z \leq 0.4$, the $H\alpha$ line is typically used for studying evolution because it can be observed optically (e.g. Ly et al. 2007; Dale et al. 2010). $H\alpha$ moves out of the optical range at $z > 0.4$ into the near-infrared (NIR). For this reason, the $[O\text{II}]$ emission line that is available in the optical out to $z \sim 1.5$ has been used instead (e.g. Zhu, Moustakas & Blanton 2009; Gilbank et al. 2010a; Bayliss et al. 2011). Previously, NIR spectrographs on large telescopes enabled observations of only a few tens of galaxies at a time at $z \sim 1$ because these were restricted to long-slit spectroscopy (e.g. Glazebrook et al. 1999; Tresse et al. 2002). Recently, the development of NIR multi-object spectrographs and wide-field NIR cameras with narrow band filters has enabled large ground-based $H\alpha$ surveys to be conducted (e.g. Geach et al. 2008; Villar et al. 2008; Twite et al. 2012; Kashino et al. 2013; Momcheva et al. 2013) out to $z \sim 2.5$. It is difficult to deal with atmospheric effects, such as seeing that blurs the image and the sky brightness that adds background noise, from ground-based observations. Space-based telescopes provide a better alternative because they are above the atmosphere and therefore exclude these effects. In particular, the much lower background in the NIR from orbit makes space particularly advantageous when compared with ground-based observations. $H\alpha$ spectroscopic surveys with *HST*, for example, provide much deeper observations than is possible from the ground (e.g. McCarthy et al. 1999; Shim et al. 2009). (With optical surveys, where we are able to work between bright sky lines, the difference between ground and space is much less pronounced.) The Wide-Field Camera (WFC3) and grism on *HST* has been used to conduct slitless spectroscopic surveys, for example 3D-*HST* (van Dokkum et al. 2011; Brammer et al. 2012) and WISP (Atek et al. 2010).

In this paper, we study a spectroscopic sample of $[O\text{II}]$ -selected dwarf galaxies by targeting the $H\alpha$ emission line using NIR slitless spectroscopy from *HST*. We determine the $H\alpha$ SFR and compare it

to the SFR derived from the $[O\text{II}]$ fluxes, confirming that the mass-dependent correction found by Gilbank et al. (2010b, hereafter G10) is necessary to reconcile the SFR indicators for these $z \sim 1$ galaxies.

This paper is presented as follows. Section 2 introduces the data used and explains how the reduction was done to extract the spectra for our sample of galaxies. A line detection algorithm was developed to analyse the extracted spectra and is described in Section 3. The algorithm produces measurements of the line luminosity that we convert into $H\alpha$ SFR measurements and compare with other SFR indicators such as the mass-dependent correction for the $[O\text{II}]$ SFR (G10) in Section 4. We show the $H\alpha$ SSFR–mass relation for galaxies at low stellar masses ($M_* < 10^{9.5} M_\odot$) in Section 4, and Section 5 presents our conclusions. All magnitudes are quoted on the AB system and we adopt a Λ CDM cosmology with $\Omega_m = 0.3$, $\Lambda = 0.7$ and $H_0 = 70 \text{ km s}^{-1} \text{ Mpc}^{-1}$. Throughout, we convert all quantities to those using a Kroupa (2001) initial mass function (IMF).

2 METHOD

2.1 Sample selection

Our galaxies are selected from the Redshift One LDSS3 Emission line Survey (ROLES; Davies et al. 2009; Gilbank et al. 2010a). ROLES was designed to specifically target K-faint ($22.5 < K_{AB} < 24$) star-forming dwarf galaxies at $z \sim 1$. ROLES obtained spectroscopy using a custom KG750 band-limiting filter on the LDSS3 spectrograph (on the Magellan II telescope) to cover the wavelength range $7500 \pm 500 \text{ \AA}$. It targeted low stellar mass galaxies ($8.5 < \log(\frac{M_*}{M_\odot}) < 9.5$) in the redshift range $0.89 < z < 1.15$ in two fields: the Great Observatories Origins Deep Survey-South (GOODS-S) field and the FIRES field. In this paper, we use only the GOODS-S data, which has overlapping WFC3 grism spectroscopy from the 3D-*HST* survey.

The $[O\text{II}]\lambda_{3727}$ emission line was used to obtain spectroscopic redshifts and $[O\text{II}]$ luminosities for estimating SFRs, down to a limit of $\sim 0.1 M_\odot \text{ yr}^{-1}$ (Gilbank et al. 2010a). The ROLES low-mass data are supplemented with an external subsample of emission line galaxies from ESO public spectroscopy (Vanzella et al. 2008) to extend their mass range up to $10^{11.5} M_\odot$ to study the mass dependence of galaxy properties such as the SSFR–mass, star formation rate density (SFRD), luminosity function, etc. at $z \sim 1$. The ESO public spectroscopic data overlap the same region of sky as ROLES and only those galaxies within the ROLES redshift range were selected. The $[O\text{II}]$ SFRs were measured in the same way as for ROLES by Gilbank et al. (2010a). To first order, the ESO public and ROLES are just different mass sub-samples of otherwise similar data. A more detailed comparison can be found in Gilbank et al. (2010a) and is also discussed in the appendix.

The full data sample (i.e. ROLES and ESO galaxies) and the sample containing ROLES galaxies only are hereafter referred to as WFC3-OII and WFC3-ROLES, respectively.

2.2 Data

The GOODS-S region is an extragalactic field well studied by many surveys, one of which is 3D-*HST*.¹ The 3D-*HST* survey obtained low-resolution NIR slitless spectroscopic data from observations taken with the WFC3/G141 grism from *HST* together with

¹ <http://3dhst.research.yale.edu/>

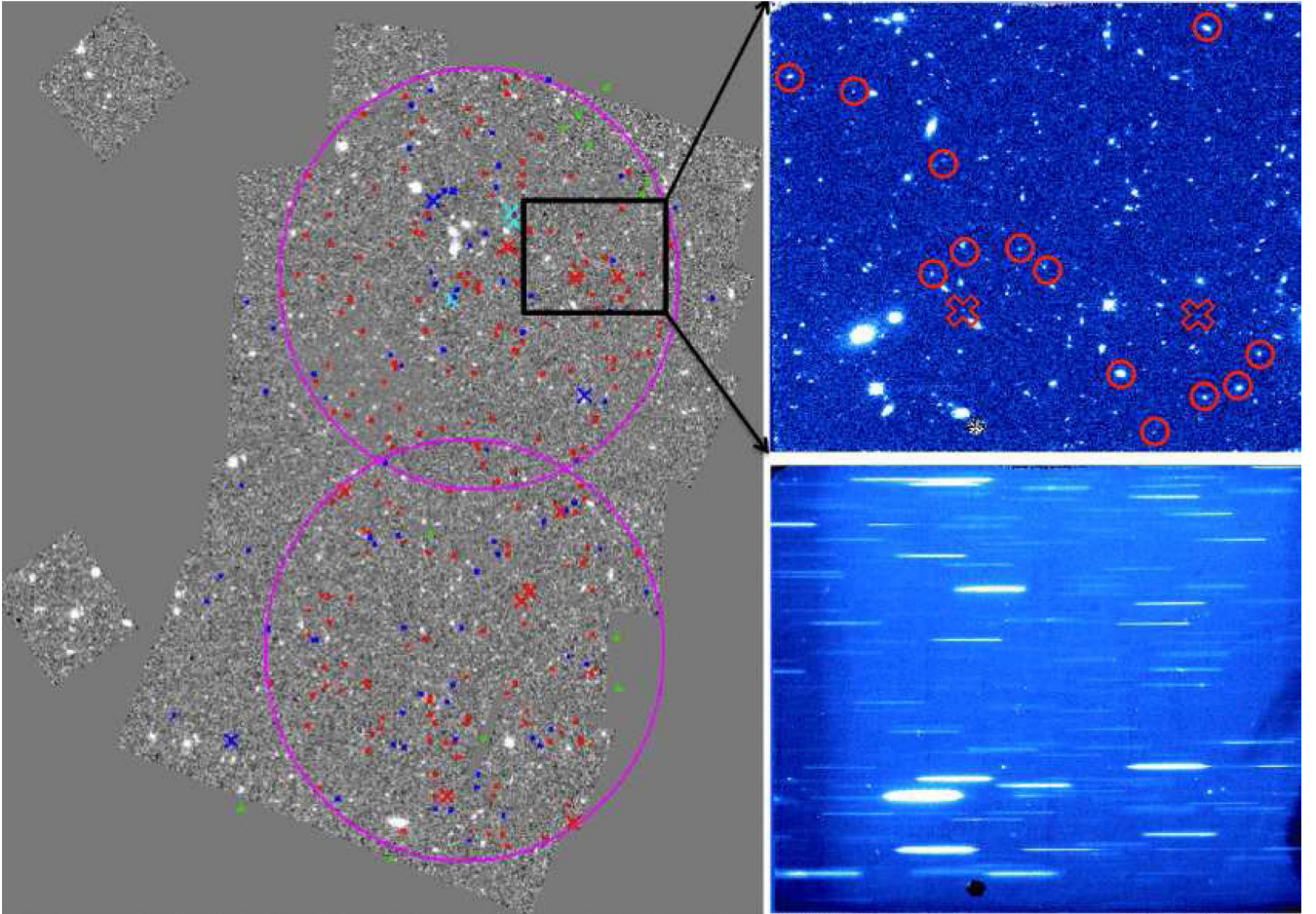


Figure 1. Direct image mosaic map (comprising 38 pointings) of the GOODS-S (RA: $3^{\text{h}}32^{\text{m}}30^{\text{s}}$, Dec: $-27^{\circ}48'54''$) region. The size of each pointing can be seen from the two outlying fields on the left of the image. The image shows the WFC3-ROLES galaxies and ESO Public spectroscopy galaxies that have a spectrum covering the $H\alpha$ wavelength range (red and blue points, respectively) and the galaxies that do not have a spectrum (red and blue crosses, respectively) covering the wavelength range where $H\alpha$ is expected. Galaxies not reduced by the spectroscopic reduction pipeline are indicated by cyan crosses. Galaxies that fall in the gaps between pointings (green circles) are excluded from the WFC3-OII sample. The ROLES footprint is indicated by two magenta circles of roughly 8 arcmin diameter. The insets show a direct image (red circles show WFC3-ROLES galaxies with spectra and red crosses show those without spectra) and the corresponding 2D slitless spectrum of a single pointing.

WFC3/F140W direct images. The GOODS-S field comprises 38 pointings, as shown by the direct mosaic map in Fig. 1. Fig. 1 shows the layout of the ROLES field with the WFC3-OII galaxies overlaid, together with a zoom-in of a single pointing and its corresponding slitless 2D spectroscopic image. We target the $H\alpha$ emission line in our [O II]-selected sample of WFC3-OII galaxies. There are 12 galaxies that fall in gaps between pointings that reduces our sample to 299 WFC3-OII galaxies.

The WFC3/G141 spectra have a wavelength coverage from approximately 11 000–16 500 Å at a spatial resolution of ~ 0.13 arcsec. (Brammer et al. 2012). The mean dispersion of the primary spectral order of the G141 grism is $46.5 \text{ Å pixel}^{-1}$ and the size of the resolution element is $\sim 100 \text{ Å}$ ($R \sim 120$ at 13 000 Å). These grism specifications enable the detection of the $H\alpha$ emission line in the redshift range $0.7 < z < 1.5$.

In this paper, we use the SED-fitted SFRs, dust extinction estimates and stellar masses from ROLES. They obtained these quantities by fitting deep multiwavelength photometry at each galaxy’s spectroscopic redshift to a grid of stellar population synthesis (SPS) models (using PEGASE.2; Fioc & Rocca-Volmerange 1997) as described in Glazebrook et al. (2004).

2.3 Data reduction and spectral extraction

We reduce the *HST* spectroscopic data using the spectral extraction software package, *AXE* (Kümmel et al. 2009). Details of the procedure are given in Brammer et al. (2012). Briefly, the task *Multidrizze* (Koekemoer et al. 2006) combines the multiple direct and corresponding slitless spectra from each pointing to obtain a deep exposure direct image and corresponding 2D slitless spectrum. The object positions are obtained by running the object detection algorithm, *SEXTRACTOR*, (Bertin & Arnouts 1996) on each combined direct image. A global background subtraction is done whereby the 2D master sky image is scaled to the background of the 2D slitless spectra and then subtracted. In slitless spectroscopy, contamination from overlapping spectra can be problematic. In *AXE*, the quantitative contamination method is used to determine the level of contamination in each spectrum. An estimate of the contaminating flux from all other sources is determined for each spectral bin using emission models. The dispersed contribution of every object to the slitless spectrum is modelled and, using the model information, the contaminating flux for each pixel is recorded and processed through the extraction process. This results in a contaminating flux

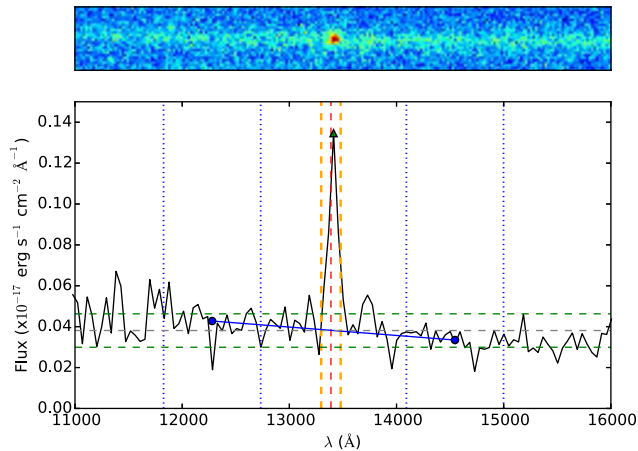


Figure 2. An example of a galaxy 2D (upper panel) and 1D spectrum extracted by the *AXE* pipeline. Bottom panel: the expected position of the emission line (dashed red line) around which the 4 pixels (~ 200 Å) window (dashed orange lines) was centred. The emission line peak (green triangle) was found within this window. The sidebands are indicated by the blue dotted lines. The blue solid line is the fit to the continuum obtained from the mean flux in the sidebands (blue circles). The green dashed lines indicate the 1σ noise level for a flat continuum (grey dashed line). The smaller peak around $13\,700$ Å is consistent with redshifted SII at $z = 1.04$. See the text for discussion.

spectrum for each extracted spectrum. Out of our selected sample of 299 galaxies, a total of 281 spectra are successfully extracted. There are 15 spectra that do not cover the wavelength range where $H\alpha$ is expected, due to their location near the edges of the detector, and a further three spectra that the *AXE* pipeline fails to extract. Fig. 2 shows an example of a 2D and 1D spectrum extracted by the *AXE* pipeline.

3 SPECTRAL ANALYSIS

We use an automated algorithm to verify the presence and measure the luminosity of the $H\alpha$ emission line for each spectrum. For this data set, we have the ROLES [O II]-based spectroscopic redshifts, which means that we know where to search for the expected wavelength of $H\alpha$.

However, we do not always expect to detect an emission line. This is because the galaxies we are targeting have very low masses and therefore low SFRs ($\sim 0.1 M_{\odot} \text{ yr}^{-1}$). We can estimate the approximate limiting SFR of the $H\alpha$ data by using the standard relation from K98 (converted to our assumed IMF) and setting this equal to the typical flux limit (3σ) of the *HST* spectra ($\sim 3 \times 10^{-17} \text{ erg cm}^{-2} \text{ s}^{-1}$). This equates to an SFR limit of $\sim 1 M_{\odot} \text{ yr}^{-1}$. This is a factor of 3 higher than the nominal ROLES' limit for [O II] that means that we do not expect to detect the lowest SFR galaxies. In addition, these galaxies are so faint that we do not expect to detect continuum for most of them. Thus, the *HST* spectra for our data set are unusual in the sense that they are mostly noise (undetected continuum), but with a fraction exhibiting a significant emission line. Furthermore, these data are unusual in that they are very low-resolution spectra (100Å), meaning that the line is unresolved. In fact, the resolution element is so wide that the $[\text{N II}]_{\lambda 6548}$ and $[\text{N II}]_{\lambda 6583}$ lines are blended with the $H\alpha$ line. To correct for the flux contribution from [N II], we assume a typical ratio of $[\text{N II}]/([\text{N II}] + H\alpha) \approx 0.25$ (Sobral et al. 2013).

3.1 Automated line detection algorithm

We briefly outline the steps our automated algorithm uses to detect and measure $H\alpha$ flux. The aspects of the 1D spectra discussed below are illustrated in the lower panel of Fig. 2.

3.1.1 Line verification

To account for uncertainty in the precise location of the emission line due to wavelength calibration of the G141 grism or the calibration used by ROLES to determine the galaxy redshifts, the algorithm begins by placing a window ~ 200 Å (4 pixels) wide centred on the expected line position. The final line position was identified as the pixel containing the highest flux within the window.²

3.1.2 Continuum estimate

The flux at the position of the line contains flux from both the line and the continuum. The latter must be estimated and subtracted from the total flux in order to determine the true line flux. This is done by calculating the continuum in two 1D sidebands on either side of the line. A width of 20 pixels, ranging from $(x_{\text{peak}} - 15)$ pixels to $(x_{\text{peak}} - 35)$ pixels and $(x_{\text{peak}} + 15)$ pixels to $(x_{\text{peak}} + 35)$ pixels, is chosen as a reasonable estimate for the sidebands. These values were chosen by visually inspecting all spectra that showed obvious emission lines, to decide first, how far from the line to position the sideband so that the line flux was not included when calculating the continuum and secondly, how wide to make the sidebands to ensure that they contained enough continuum flux such that a linear fit to the continuum was valid.

3.1.3 Line luminosity measurement

The final step in the algorithm is to measure the line luminosity and its uncertainty. The line has some width, so to calculate the total flux of the line, we have to integrate over a finite region. Choosing an integration region was a trade-off between including too much noise by making the region too wide and not including all the emission line flux by making the region too narrow. To determine how wide a region to integrate over, spectra were visually inspected and a width of 480 Å (10 pixels), centred on the peak of the emission line, was chosen as a reasonable estimate. The line luminosity was then calculated using

$$L(H\alpha) = 4\pi F(H\alpha)(D_L^2), \quad (1)$$

where $F(H\alpha)$ is the integrated flux of the emission line after continuum subtraction and D_L is the luminosity distance (e.g. Hogg 1999).

The uncertainty on the flux, σ is calculated as the standard deviation integrated over a region of the same width as the integration region of the emission line (10 pixels or 480Å). The noise just takes into account noise from the continuum and not Poisson noise from the emission line itself. For bright lines, the noise will be misestimated, but here we care primarily about the detection of faint lines where the Poisson noise from the line itself will be low.

² The (internal) precision of the ROLES [O II] redshifts is 100 km s^{-1} observed frame Gilbank et al. (2010a), so in principle a one WFC3 pixel window would be sufficient. However, since we use a 10 pixel window to measure the integrated flux (described below) in practice it makes negligible difference to the final flux whether we use a one or four pixel centring box.

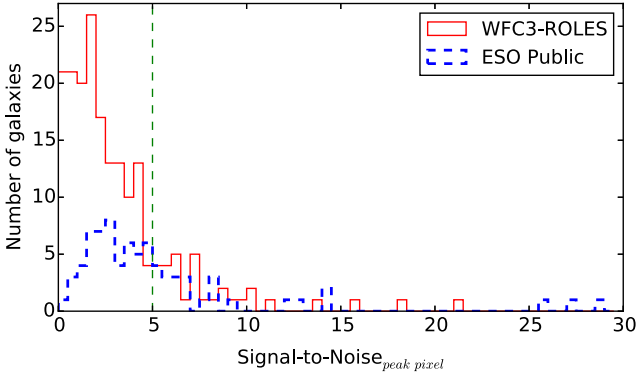


Figure 3. Distribution of the significance of the emission lines for all 281 unique galaxies in the sample separated into WFC3-ROLES (red) and ESO Public Spectroscopy galaxies (blue). This shows the relative number of detections and limits expected for any chosen $(S/N)_{\text{peak}}$ threshold (the green dashed line shows our chosen detection threshold of $(S/N)_{\text{peak}} \geq 5$). Objects with an $(S/N)_{\text{peak}}$ greater than the threshold are considered detections and those less than the threshold are limits.

3.1.4 S/N of detections

In order to determine the significance of detections, we adopt a slightly more conservative approach than for the flux measurements. We define the signal to noise relative to the peak pixel in the detection. The S/N ratio is then calculated as

$$(S/N)_{\text{peak}} = \frac{F_{\text{peak}}(H\alpha)}{\sigma_{\text{per pixel}}} \quad (2)$$

where $F_{\text{peak}}(H\alpha)$ is the flux in the peak pixel of the emission line after continuum subtraction and $\sigma_{\text{per pixel}}$ is the noise per pixel of the spectrum, calculated from the side bands as above.

As described above, our estimate of $(S/N)_{\text{peak}}$ is mostly used as an approximation to rank order detections, rather than a detailed estimate of the noise (as calculated from the continuum noise above, for example). As with ROLES, we found the best method to assess significance of detections was a combination of visual inspection and reproducibility of detections in repeated observations.

As mentioned before, we do not always expect to detect an emission line. For this reason, a detection threshold has to be defined for our sample. Choosing a detection threshold is a trade-off between purity and completeness. A very high threshold means that one has a pure sample that is incomplete (i.e. missing real detections). On the other hand, as one moves to lower thresholds, the sample becomes more complete but the probability of including spurious detections increases. An $S/N \geq 5$ is chosen as the detection threshold from a combination of visual inspection and testing the reproducibility of automated detections (detailed in Appendix A). The distribution of $(S/N)_{\text{peak}}$ of the 281 WFC3-OII galaxies is shown in Fig. 3. Using this threshold, we obtain 56 detections.

4 RESULTS AND DISCUSSION

4.1 Dust extinction correction

In order to convert from a measured $H\alpha$ luminosity into an SFR, it is necessary to have an estimate of the dust extinction. Unfortunately, our spectra do not cover the wavelength range of the $H\beta$ emission line, which means that the dust extinction cannot be measured using the Balmer decrement ($H\alpha/H\beta$) as is commonly done (e.g. Kashino et al. 2013). Instead, we use SED fits to estimate the dust extinction, A_V , and compare our measurements to other studies, where the dust extinction has been measured using the Balmer decrement.

Since dust is created in stars, one might expect dust extinction to depend on the number of stars (stellar mass), and/or the rate at which they are formed (SFR), in a galaxy. Previous studies (using $H\alpha/H\beta$ to measure dust) have shown that dust extinction correlates with stellar mass (e.g. G10; Garn & Best 2010; Sobral et al. 2012; Kashino et al. 2013; Momcheva et al. 2013) and $H\alpha$ luminosity (or SFR) (e.g. Hopkins et al. 2001; Pérez-González et al. 2003; Buat et al. 2005; Schmitt et al. 2006; Caputi et al. 2008).

We calculate extinction assuming a Calzetti et al. (2000) law for the continuum, A_V (A_{stars}), and SMC for the nebular emission, $H\alpha$ (A_{gas}) (e.g. Steidel et al. 2014). While Calzetti et al. advocate a ratio between A_{stars} and A_{gas} of 0.44 to allow for the differential attenuation between the two regions, i.e.

$$A_{H\alpha} = \frac{k_{H\alpha}}{k_V} \frac{A_V}{0.44} = 1.8673 A_V, \quad (3)$$

(where $k_{H\alpha} = 3.3258$ and $k_V = 4.04789$), other works argue that the factor of 0.44 appearing in the denominator of equation (3) may depend on the properties of the galaxies and growing evidence at $z \sim 1$ suggests that the additional extinction suffered by the gas relative to the stars should be lower than the Calzetti value. For example, Price et al. (2014), Reddy et al. (2015), Wuyts et al. (2013) with some values ranging as low as no additional extinction (e.g. Kashino et al. 2013, or $A_{\text{gas}} = A_{\text{stars}}$).

$$A_{H\alpha} = 0.822 A_V. \quad (4)$$

For simplicity, we begin by assuming equal extinction between stars and gas as a lower limit, but explore some of the alternative suggested parametrizations as a function of stellar mass. In Fig. 4, we plot our SED-fitted dust estimates using equation (4) as a function of stellar mass. For comparison, the median dust extinction and stellar mass values of Momcheva et al. (2013), Sobral et al. (2012) and Kashino et al. (2013) are plotted together with the local relations derived by Garn & Best (2010) and G10 at $z \sim 0.1$ given by the following, respectively:

$$A_{H\alpha} = 0.91 + 0.77 X + 0.11 X^2 - 0.09 X^3 \quad (\text{Garn \& Best 2010}), \quad (5)$$

where $X = \log(M_*/10^{10}M_\odot)$, and

$$A_{H\alpha} = a + b \log(M_*/M_\odot) + c [\log(M_*/M_\odot)]^2, \quad (\text{G10}) \quad (6)$$

where $a = 51.201$, $b = -11.199$, $c = 0.615$ and is set to a constant value for $\log(M_*/M_\odot) \leq 9.0$.

The Momcheva et al. (2013) sample at $z \sim 0.8$ is the closest to our redshift range. For low-mass galaxies ($\log(M_*/M_\odot) < 10$), our dust estimates agree well with the median Balmer decrement dust measurements of Momcheva et al. (2013) within the uncertainties. Furthermore, our dust estimates for low masses fall on the local relations of Garn & Best (2010) and G10, both derived using SDSS data. At the highest masses, however, our measurements begin to fall below the G10 relation locally and also the highest mass data point at $z \sim 1.5$ Kashino et al. (2013). The highest mass point of Momcheva et al. (2013) is offset even further below the local relation. They mention that this data point may have possible contamination by their stacked sample due to unidentified AGN at this mass range. However, our data agree well with the Sobral et al. (2013) measurements at $z \sim 1.45$ and are consistent with the Garn & Best (2010) local relation.

In the right-hand panel of the figure, we explore some of the alternate parametrizations of $A_{H\alpha}$ as a function of stellar mass. In addition to the Calzetti et al. (2000) relation and our equal extinction in stars and gas relation (essentially $0.44A_{H\alpha, \text{Calzetti}}$), we use the relation from Wuyts et al. (2013), $A_{\text{gas}} = 1.9A_{\text{stars}} - 0.15A_{\text{stars}}^2$;

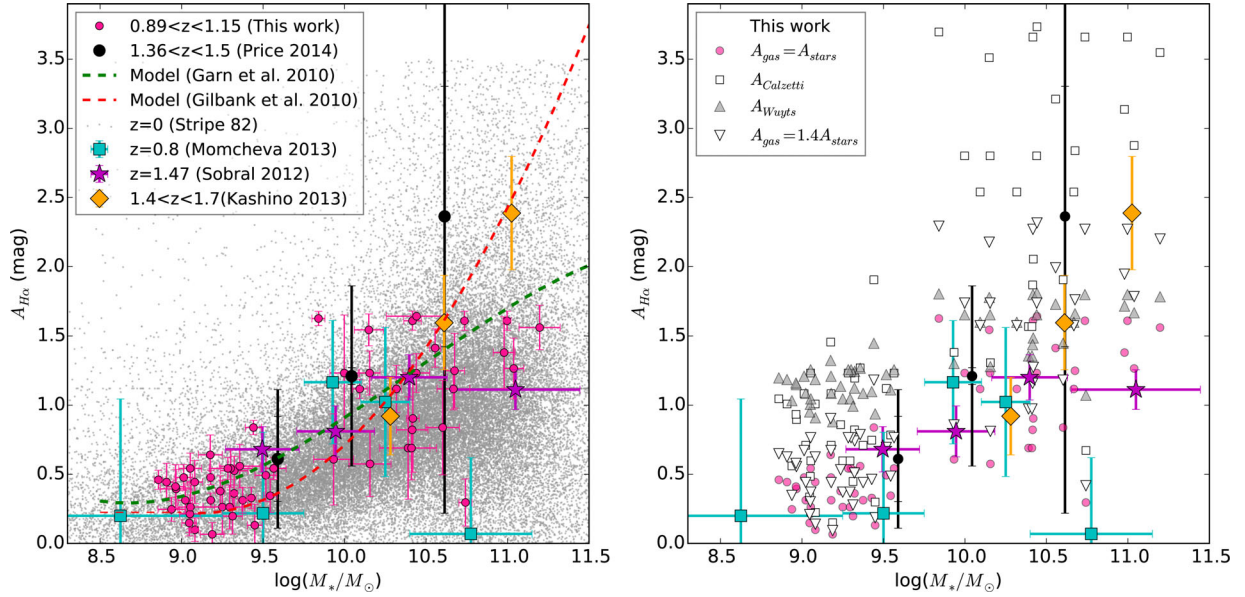


Figure 4. The relation between dust extinction ($A_{H\alpha}$) and stellar mass. All external comparison samples estimate dust using the Balmer decrement. Our SED-fitted dust estimates (pink points) for the low-mass galaxies agree well with the Momcheva et al. (2013) data at a similar redshift and also with local relations derived from SDSS data. Small, grey points show (Balmer decrement based) measurements from SDSS. The right-hand panel repeats the $z \sim 1$ observations from the left-hand panel (coloured points) and compares with four different scalings of dust extinction for our data (grey points, error bars omitted for clarity). See the text for discussion.

and $A_{\text{gas}} = 1.4A_{\text{gas}}$ that is an approximation to the relation found by Reddy et al. (2015). The latter relation seems to bring our data points closest to the observed Balmer decrement measurements found in other works, but $A_{\text{gas}} = A_{\text{stars}}$ is also in reasonable agreement, if somewhat lower than Kashino et al. (2013) at the highest masses. Using Wuyts et al. (2013) relation, our lowest mass galaxies significantly exceed the extinction predicted by other works (Sobral et al. 2012; Momcheva et al. 2013), and the Calzetti correction significantly overpredicts the extinction in the highest mass galaxies, as found by other works. For simplicity, we choose to use $A_{\text{gas}} = A_{\text{stars}}$ (equation 4) throughout, but will discuss the differences these other reasonable choices, particularly $A_{\text{gas}} = 1.4A_{\text{stars}}$ would make to our results.

4.2 SFR indicators

In this section, we examine all the SFR estimators available for use with our data. These comprise three indicators ($H\alpha$, $[O\text{II}]$ and SED fitting), each with various possible assumptions and corrections. Each of these has its own advantages and disadvantages, including different sensitivities to factors such as dust, metallicity, as well as the time-scales to which it is sensitive. A more thorough discussion can be found in G10.

As we have shown in the previous section, using $A_{H\alpha}$ estimated from the SED-fitted continuum extinction, scaled as described in equation (4) gives reasonable agreement with the Balmer decrement based $A_{H\alpha}$ values from other studies at similar redshifts. Thus, we use this as our fiducial scaling and test the calibration of other available indicators against this.

4.2.1 $H\alpha$ SFR

We calculate the $H\alpha$ SFR using

$$\frac{\text{SFR}}{[M_\odot \text{ yr}^{-1}]} = \frac{10^{0.4A_{H\alpha}}}{1.5} \frac{L(H\alpha)}{1.27 \times 10^{41} [\text{erg s}^{-1}]}, \quad (7)$$

where $A_{H\alpha}$ is calculated using equation (4) and $L(H\alpha)$ is the measured $H\alpha$ line luminosity (see Section 3.1.3). This is the K98, K98, relation divided by a factor of 1.5 to convert from a Salpeter IMF to a Kroupa (2001) IMF.

4.2.2 Nominal $[O\text{II}]$ SFR ($[O\text{II}]K98$)

The SFR measured from $[O\text{II}]$ luminosity was calibrated by K98 by scaling between the $[O\text{II}]$ and $H\alpha$ luminosity as

$$\frac{\text{SFR}}{[M_\odot \text{ yr}^{-1}]} = \frac{L([O\text{II}])}{2.53 \times 10^{40} [\text{erg s}^{-1}]}. \quad (8)$$

The original scaling was determined by K98 from the $H\alpha$ SFR and so the normalization constant assumes nominal values for the extinction and ratio of $H\alpha/[O\text{II}]$ luminosity, etc. Our intention here with the $[O\text{II}]K98$ method is to just use the nominal scaling from $[O\text{II}]$ luminosity, as would be used in the absence of other measurements such as extinction, metallicity, etc. to see how well this compares with the other estimators. Due to the relative ease of obtaining $[O\text{II}]$ SFRs versus $H\alpha$ at these redshifts, $[O\text{II}]$ is still an important tracer of SFR (see G10 for further discussion).

4.2.3 Empirically corrected $[O\text{II}]$ SFR ($[O\text{II}]G10$)

The empirically corrected $[O\text{II}]$ SFR (referred to as $[O\text{II}]G10$) is calculated using the G10 mass-dependent empirical correction,

$$\frac{\text{SFR}_{\text{emp,corr}}}{[M_\odot \text{ yr}^{-1}]} = \frac{L([O\text{II}])}{2.53 \times 10^{40}} \frac{1}{(a \tanh[(x-b)/c] + d)}, \quad (9)$$

where $x = \log(M_*/M_\odot)$, $a = -1.424$, $b = 9.827$, $c = 0.572$, $d = 1.700$ and $L([O\text{II}])$ is the $[O\text{II}]$ emission line luminosity.

As mentioned, the nominal luminosity scaling of $[O\text{II}]K98$ method is sensitive to various factors such as dust extinction, metallicity, ionization parameter, etc. G10 attempted to correct for these

by parametrizing the combined dependence of all these factors empirically as a function of stellar mass.

4.2.4 SED-fitted SFRs

SED-fitted SFRs are calculated from the same procedure as our stellar masses. The method used is that detailed in Glazebrook et al. (2004), fitting the extensive multiwavelength photometry (see G10)

at the spectroscopic redshift to a grid of PEGASE.2 (Fioc & Rocca-Volmerange 1997) stellar population models.

4.3 $H\alpha$ and $O\text{II}$ SFR COMPARISON

In Fig. 5, we begin by comparing the nominal (K98) scalings between $H\alpha$ and $[O\text{II}]$. These are essentially direct scalings from line luminosities and so are closest to the raw data. The top left panel

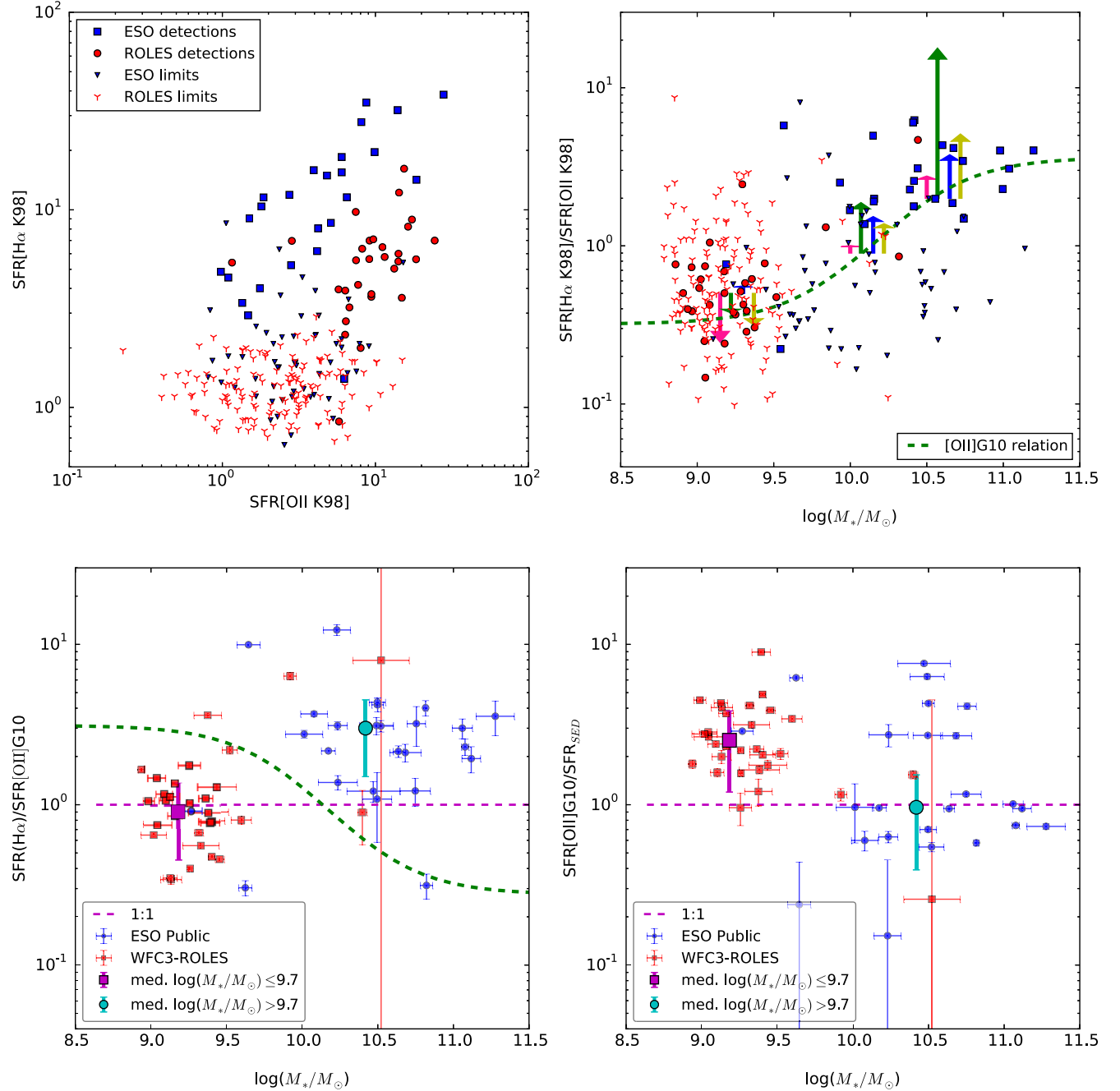


Figure 5. Upper left panel: the comparison between SFRs directly scaled from luminosity (K98) for $H\alpha$ and $[O\text{II}]$. Larger symbols indicate $H\alpha$ detections and smaller symbols denote upper limits in $H\alpha$. Upper right panel: the ratio of the K98 SFRs as a function of stellar mass, symbols as previous panel. The dashed relation indicates the empirical mass-dependent correction for $[O\text{II}]$ SFR (G10). Arrows indicate the change in SFR by adopting the different dust correction schemes (from left to right: $A_{\text{gas}} = A_{\text{stars}}$, A_{Calzetti} , A_{Wuyts} , $A_{\text{gas}} = 1.4A_{\text{stars}}$) for three representative mass bins. See the text for discussion. Lower left panel: the ratio of the (extinction-corrected) $H\alpha$ and $[O\text{II}]G10$ SFR relations as a function of stellar mass. The G10 empirical correction fixes most of the mass-dependent trend that would be present if only a constant conversion from $[O\text{II}]$ luminosity to SFR is used (dashed green line). Lower right panel: the $[O\text{II}]G10$ SFR and SED-fitted SFR ratio as a function of stellar mass shows a small residual trend with mass. See the text for discussion.

shows a correlation between the two line luminosities albeit with significant scatter. In addition, for the detections (larger points) there seems to be a systematic offset between the ROLES (lower mass) and ESO (higher mass) measurements. In the upper right panel, the ratio of the line luminosities is shown as a function of stellar mass. The mass-dependent offset is now clearer, and as can be seen from the dashed line, the empirical correction to the $[\text{O II}]$ SFR (G10) corrects for the bulk of the offset prior to any additional corrections (such as mass-dependent extinction) in the $\text{H}\alpha$ data, although the scatter is still broad. To illustrate the effect of the different dust corrections explored in the previous section, the arrows indicate the change in $\text{H}\alpha$ SFR for typical nominal $\text{H}\alpha$ SFRs at three representative masses, relative to the K98 $A_{\text{H}\alpha} = 1.0$ mag correction. It can be seen that the dust-corrected $\text{H}\alpha$ SFRs are reduced at the lowest masses, and increase by differing amounts at higher masses, with the Calzetti correction leading to the highest increase, and our adopted $A_{\text{gas}} = A_{\text{stars}}$ giving the smallest increase. In the highest mass bins, the agreement between our adopted measurement and the two other alternatives is much closer than their agreement with the Calzetti relation.

In the lower left panel of Fig. 5, we plot the ratio of the (extinction-corrected) $\text{H}\alpha$ and the empirically corrected $[\text{O II}]$ G10 SFRs as a function of stellar mass. The dashed line shows where the data would fall if this correction is not applied and the nominal (constant) conversion from $[\text{O II}]$ luminosity to SFR (K98) is used instead. Clearly, this would leave a residual mass trend between the high- and low-mass galaxies, as is also seen from the upper right panel: most of the discrepancy between $\text{H}\alpha$ luminosity-inferred SFR and $[\text{O II}]$ luminosity-inferred SFR is reconciled by this mass-dependent correction. The motivation for this correction is given in G10 and the likely applicability at $z \sim 1$ is discussed in Gilbank et al. (2010a). Briefly, the conversion from $[\text{O II}]$ luminosity to SFR depends on gas phase metallicity, dust extinction and ionization parameter (e.g. Kewley, Geller & Jansen 2004). Several workers have invoked empirical corrections to $[\text{O II}]$ SFRs based on broad-band luminosities or stellar masses. In as much as the mass-dependent scaling of these various contributions remain approximately constant (or even evolve but in opposing directions so as to cancel out), the empirical relation derived at $z \sim 0.1$ might also be expected to work at $z \sim 1.0$. A full exploration of the applicability of this correction is difficult, given the limited data available (individual galaxies spanning a range of stellar masses with $[\text{O II}]$, $\text{H}\alpha$ luminosity measurements and reliable individual dust measurements), but we can estimate how much the G10 relation might evolve by $z \sim 1$ by looking at the measured evolution in the mass–metallicity relation (e.g. Savaglio et al. 2005) and the mass–extinction relation (e.g. Fig. 4).³ From Savaglio et al. (2005), at a fixed metallicity, the corresponding stellar mass changes by $\log(M_*) \lesssim 0.4$ between the local Universe and their high-redshift bin ($z \sim 0.7$). The bulk of the high- and low-mass galaxies in this sample lie on the flat parts of the tanh correction curve, and so choosing a correction from $\log(M_*) \sim 0.4$ away makes little difference to the correction factor. Or, alternatively, metallicity decreases by ~ 0.1 – 0.2 dex at fixed stellar mass up to this redshift. The decrease in metallicity means a higher $[\text{O II}]/\text{H}\alpha$ luminosity at a given SFR (e.g. Kewley et al. 2004), implying a given $[\text{O II}]$ luminosity would overestimate the SFR using a fixed luminosity conversion. This may be partly cancelled by

an increase in dust extinction relative to $z \sim 0$ (Fig. 4). Thus, it is not unreasonable that the local empirical correction could also apply at $z \sim 1$. Its original motivation was to correct for biases in measurements of SFR and SFR density at $z \sim 1$ as a function of stellar mass using $[\text{O II}]$ as the only SFR indicator (Juneau et al. 2005), and so part of the motivation was to use a mass-dependent correction since this quantity was always available as part of the studies. Whether it is the best or observationally cheapest proxy for such studies is a separate question. Reddy et al. (2015) favour SSFR-based scalings in order to infer dust corrections at $z \sim 1.5$, and so similar scalings will be important in the near future in order to maximally extract information from such studies where individual estimates of all relevant quantities may not be available individually for each galaxy.

Most of the WFC3-ROLES data (almost exclusively low-mass galaxies, by design) lie below the K98 relation, whereas most of the ESO Public data (higher mass galaxies) lie above the K98 relation. The median ratio of the lower mass data (mostly WFC3-ROLES data) is 0.29 ± 0.15 (0.80 ± 0.36) without (with) this empirical correction and the median for the higher mass data (mostly ESO Public data) is 3.59 ± 2.78 (1.94 ± 1.01) without (and with correction, respectively). There is more scatter in the high-mass data than the low-mass data which means that the data is less well constrained at high masses. Most interesting is that the ratio as a function of mass follows the mass-dependent correction of G10 derived at low redshift (equation 9, purple line) within the uncertainties. This shows us that it is necessary to apply the mass-dependent $[\text{O II}]$ G10 correction to $[\text{O II}]$ SFRs rather than simply assuming a constant $[\text{O II}]$ luminosity to SFR conversion. Furthermore, this confirms that the $[\text{O II}]$ G10 relation at $z \sim 1$ is consistent with the normalization found at $z \sim 0.1$. We cannot, however, rule out moderate evolution in this correction, given the broad uncertainties of our $z \sim 1$ $\text{H}\alpha$ measurements.

4.4 Comparison with SED-fitted SFRs

We now compare the ratio of the SED-fitted SFRs and $[\text{O II}]$ SFRs as a function of stellar mass in the right-hand panel of Fig. 5. (The ratio between $\text{H}\alpha$ and SED-fitted SFRs can similarly be inferred from the combination of the two, given the agreement between $[\text{O II}]$ G10 and $\text{H}\alpha$.) The ratio of the SFRs for the high-mass bin is consistent with unity (1.0 ± 0.9); however, for the low-mass bin, the ratio is 0.4 ± 0.2 , suggesting a slight residual trend for SED-fitted SFRs relative to $[\text{O II}]$ G10 or $\text{H}\alpha$. This is in contrast to Gilbank et al. (2010a) who found that the SED-fitted SFRs are approximately 1.7 times higher than $[\text{O II}]$ G10 for ROLES. This could be due to sample selection in the current comparison. Since we only compare objects with significant $\text{H}\alpha$ detections, if the $[\text{O II}]$ (or $\text{H}\alpha$)–SFR relation has moderate scatter, an Eddington-like bias could lead us to pre-select only the high $\text{H}\alpha$ (or $[\text{O II}]$) outliers in $\text{H}\alpha$ versus SED in this comparison.

Other studies have used the $[\text{O II}]$ G10 empirical correction. Mostek et al. (2012) showed how $[\text{O II}]$ G10 correction compares to SFRs measured at $z \sim 1$ using SFR fits from the UV/optical SEDs in the AEGIS survey. They found that the SED-fitted SFRs and the $[\text{O II}]$ G10 empirically calibrated SFRs agree with 0.27 dex (1.86) scatter and have a mean offset of -0.06 dex (0.87). Mok et al. (2013) used the $[\text{O II}]$ G10 correction to obtain SFRs for a sample of galaxy groups from the Group Environment Evolution Collaboration 2 (GEEC2; Balogh et al. 2011). They compared the SFRs derived from this method to SFRs calculated from using FUV SED fits combined with $24\text{ }\mu\text{m}$, which should trace the total

³ Remember these components are not fitted individually in the G10 derivation, only the overall contribution of all terms including ionization parameter, for which we do not have measurements for these galaxies.

(obscured and unobscured) star formation in the galaxy. They noticed a systematic normalization offset between the two indicators. They found that the $[\text{O II}]$ SFR estimated using $[\text{O II}]\text{G10}$ is underestimated by a factor of 3.1, much larger than the offset found here and by the other cited works.

4.4.1 Possible systematic uncertainties

The two main sources of uncertainty in our $H\alpha$ SFRs are the $[\text{N II}]$ correction to the blended ($H\alpha + [\text{N II}]$) flux and the correction for dust extinction. We used an average $[\text{N II}]/(H\alpha + [\text{N II}])$ correction of 0.25 that corresponds to an $[\text{N II}]/H\alpha$ of 0.33 and is close to the values derived by Sobral et al. (2012) and Sobral et al. (2013) at these redshifts, and is the same as the conventionally used 33 percent in $[\text{N II}]/H\alpha$. Some studies have shown that the $[\text{N II}]/H\alpha$ ratio increases with stellar mass (e.g. Erb et al. 2006). Furthermore the ratio, at any particular stellar mass, evolves with redshift (e.g. Erb et al. 2006). If the ratio has been overestimated for the low-mass galaxies and underestimated for the high-mass galaxies, it could result in the slight residual trend seen in our data in the left-hand panel of Fig. 5. Typically, used $[\text{N II}]/H\alpha$ ratios are in the range 0.3–0.5 (Kennicutt & Kent 1983; Kennicutt 1992). Applying the extremes of the ratio to the data, bring the $H\alpha$ and $[\text{O II}]$ SFR ratios close to unity as possible but there still is a residual trend. Our result of a mass-dependent difference between $H\alpha$ and $[\text{O II}]$ is therefore robust to any reasonable choice of $[\text{N II}]/H\alpha$ correction.

In order to investigate the effects that our choice of dust extinction estimate has on the differing ratios of SFRs for high- and low-mass galaxies, we look at a range of possible extinction estimates by considering the alternative dust extinction laws discussed in Section 4.3. The recomputed numbers for the dust-corrected $H\alpha/[\text{O II}]\text{G10}$ SFR ratios (the lower left panel of Fig. 5, given in Section 4.3) using A_{Wuys} or $A_{\text{gas}} = 1.4A_{\text{stars}}$ give instead: 1.60 ± 0.74 and 0.91 ± 0.46 for the low mass bin and 2.60 ± 1.30 and 3.00 ± 1.50 for the high-mass bin, respectively. The latter being only marginally inconsistent (at $\lesssim 1.5\sigma$) with the prediction of the G10 correction.

4.5 Stacking of nondetections

To further investigate the spectra where we do not detect $H\alpha$, we stack these spectra in three bins in stellar mass (tabulated in Table 1). We first wish to test if we are able to make a significant detection from these data. Thus, to ensure that the final spectrum is not dominated by one or two detections close to our nominal threshold of 5.0σ , we only stack spectra with an $(S/N)_{\text{peak}} < 4.5$. All spectra in a given mass bin are first shifted to a reference wavelength of 13 500 Å (corresponding to a redshift, $z_{\text{ref}} = 1.057$), which is the centre of the G141 grism wavelength coverage. For each stellar mass bin, each spectrum is scaled in flux relative to the luminosity distance using z_{ref} . The spectra are then summed and divided by the number of spectra. The stacked spectra are analysed as described in Section 3 to obtain the line luminosity and its total $(S/N)_{\text{peak}}$ (equation 2). In

Table 1. For $(S/N)_{\text{peakH}\alpha} < 4.5$ detections, the sizes of the mass bins and the number of galaxies they contain, the number of stacked spectra, and the $(S/N)_{\text{peak}}$ of the stacked spectrum in each mass bin.

Bin width ($\log(M_*/M_\odot)$)	N_{spec}	$(S/N)_{\text{peak}}$
8.6–9.5	40	23.5
9.5–10.5	43	42.2
10.5–11.5	6	4.9

Table 2. The sizes of the mass bins and the number of galaxies they contain together with the median SSFR for each mass bin.

Bin width ($\log(M_*/M_\odot)$)	N_{gal}	Median SSFR (yr^{-1})
$H\alpha$ detections only		
8.6–9.5	28	-8.60 ± 0.09
9.5–10.5	16	-9.13 ± 0.11
10.5–11.5	12	-9.34 ± 0.14
Stack		
8.6–9.5	60	-8.93 ± 0.09
9.5–10.5	39	-9.58 ± 0.10
10.5–11.5	12	-9.77 ± 0.29

all the stacked spectra, we are able to detect a significant $H\alpha$ line. The aperture used for measuring the flux is sufficiently wide that the residual wavelength uncertainties (Section 3.1.1) do not affect the summed flux measured within it. The $(S/N)_{\text{peak}}$ of these three average spectra are higher than our detection threshold meaning that we could use these as extra data points in each of the mass bins when calculating the SSFR. Table 1 gives the $(S/N)_{\text{peak}}$ and number of stacked spectra for each mass bin.

5 THE SSFR–MASS RELATION AT $z \sim 1$

With these measurements in hand, we can now turn our attention to the SSFR–mass relation at $z = 1$. The SSFR is simply computed by dividing the $H\alpha$ SFR measurement by the galaxy’s stellar mass. First, we consider the impact of the non-detections on the average relation measured. Next, we compare with other (shallower) works using $H\alpha$ at similar redshifts, and finally we compare our measurements with the recent results from state-of-the-art numerical simulations (EAGLE,⁴ Furlong et al. 2015; Schaye et al. 2015).

The average relation is found by taking the median SSFR in bins of mass, as tabulated in Table 2. In order to account for the impact of non-detections, we construct a weighted stack by combining the stacked spectra described above with the individual detections at higher S/N. This is our main result and shown as the cyan points in Fig. 6. The scatter on these measurements is estimated by bootstrap resampling the data in each bin, treating all data points as detections whether formally detections or limits. This should provide a not unreasonable estimate of the uncertainty on the average relation.

A number of works have recently attempted to make either narrow-band or spectroscopic measurements of $H\alpha$ SFRs at these redshifts and their published measurements are also shown in Fig. 6. The HiZELS (The High-Redshift Emission Line Survey) study by Sobral et al. (2009, 2011) used deep NIR narrow-band imaging in J , H and K bands with the WFC at UKIRT. Sobral et al. (2012) built on the samples detected in individual bands by using a matched $H\alpha + [\text{O II}]$ dual narrow-band survey to obtain a wide-field sample at $z \sim 1.5$. In order to obtain deeper data over a wider area, Fumagalli et al. (2012) used 3D-*HST* space-based spectroscopic data to study a mass-selected sample of galaxies between $0.8 < z < 1.2$. The samples closest to our redshift range are the Fumagalli et al. (2012) and Sobral et al. (2011) at $z \sim 0.9$ and $z = 1$, respectively. In the highest mass bins, our results are consistent. However, when moving towards lower stellar mass, it is clear that our results (even for the detections only) lie systematically below other works. This is due to the greater depth of our survey and incompleteness in the other surveys. Sobral et al. (2011) note that their sample selection is

⁴ The public data base is accessible via <http://icc.dur.ac.uk/Eagle/>.

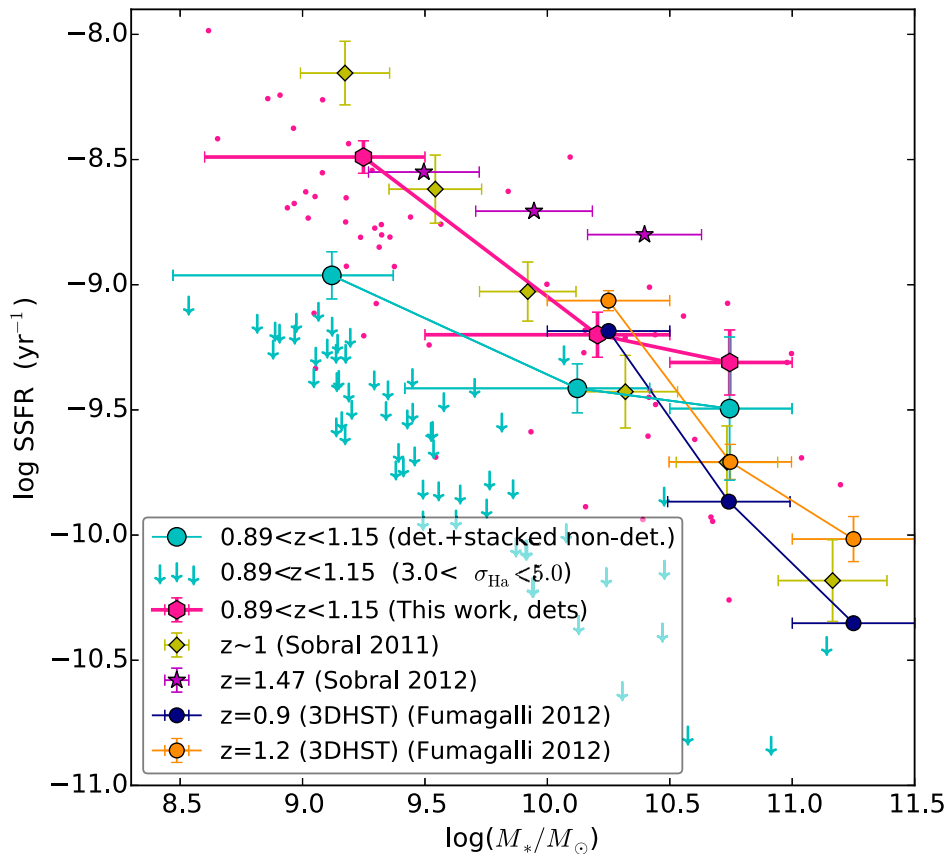


Figure 6. SSFR–mass relation where the SSFR has been measured with $H\alpha$. (For consistency, the 3D-*HST* points from Fumagalli+ have been corrected for [N II] contamination in the same way as described for our data.) We compare our median SSFR (detection) measurements (pink circles; individual galaxies shown as pink points) and stacked results including non-detections (cyan circles and upper limits) to the measurements from Fumagalli et al. (2012, navy and orange circles), Sobral et al. (2011, yellow diamonds) and Sobral et al. (2012, magenta stars). Our data probe to much lower (~ 1 dex) SSFRs than existing spectroscopic samples at similar redshifts and our stacked measurement indicates the flattening of the SSFR data missed by shallower (incomplete) samples. See the text for discussion and also next figure.

restricted to a fixed SFR limit of $> 3 M_{\odot} \text{ yr}^{-1}$. At the lowest masses probed, low-SSFR galaxies fall below their selection limit, biasing their median SSFRs upwards. They found that this bias becomes significant at masses below $\sim 10^{10} M_{\odot}$. Hence, our sample gives a better SSFR measurement for the low-mass (low-SFR) galaxies. Similarly, Fumagalli et al. (2012), who also used *HST* WFC3 grism data, only probed massive galaxies ($> 10^{10} M_{\odot}$) at a detection limit corresponding to $\text{SFR} = 2.8 M_{\odot} \text{ yr}^{-1}$.⁵

One point worth emphasizing in our study is the greater depth achievable with the *same* WFC3 grism data by pre-selecting galaxies based on the ROLES’ [O II] spectroscopic redshifts and by stacking those objects not formally detected individually. This can also be seen by comparison with the recent public release of the 3D-*HST* (Momcheva et al. 2015) spectroscopic catalogue. See comparison in Appendix C.

It is clear from this figure that the steep slope of the SSFR–stellar mass relation depends greatly on the depth of the data used. Given the difficulty in detecting weak $H\alpha$ sources, this is not surprising, and it emphasizes the point that complete samples are vital.

⁵ Applying a cut of $\text{SFR} > 3 M_{\odot} \text{ yr}^{-1}$ to our data brings our measurements closer to the other two measurements in the lowest mass bin, but does not entirely explain the difference. The point is moved by ~ 0.1 dex. In the higher mass bins, the points are essentially unchanged.

Table 3. The slopes of the SSFR–mass relation for some of the results shown in Figs 6 and 7. Representative examples are taken at $z \sim 1$, except the Stripe 82 work taken as a local comparison. See the text for discussion.

Sample	SSFR–mass slope, α
This work, detections	-0.50 ± 0.04
This work, stack	-0.47 ± 0.04
Sobral et al. (2011) ($z \sim 1$)	-1.00 ± 0.07
EAGLE ($z \sim 1$)	-0.14 ± 0.05
Stripe 82 ($z \sim 0.1$), $\log(M_*) < 10$	-0.08 ± 0.01

To illustrate this, faint-end slope power law fits ($\text{SSFR} \propto M_*^{\alpha}$) for representative sample are given in Table 3. As can be seen, the literature work, such as Sobral et al. (2011), gives $\alpha \approx -1.0$. We measure flatter slopes of $\alpha = -0.50 \pm 0.04$ for our detections only, and $\alpha = -0.47 \pm 0.04$ for our stack. Fortunately, the greater depth of our ROLES’ OII detections allows us to obtain the average $H\alpha$ of a complete sample. Our conservative $A_{\text{gas}} = A_{\text{stars}}$ dust scaling probably leads to a steeper slope than in reality, as it likely underestimates the size of the correction (and hence the SSFR) at the highest stellar masses. Applying the alternative dust corrections of A_{Wuyts} and $A_{\text{gas}} = 1.4 A_{\text{stars}}$ negligibly changes the results, giving values of $\alpha = -0.46 \pm 0.05$ and -0.46 ± 0.04 , respectively.

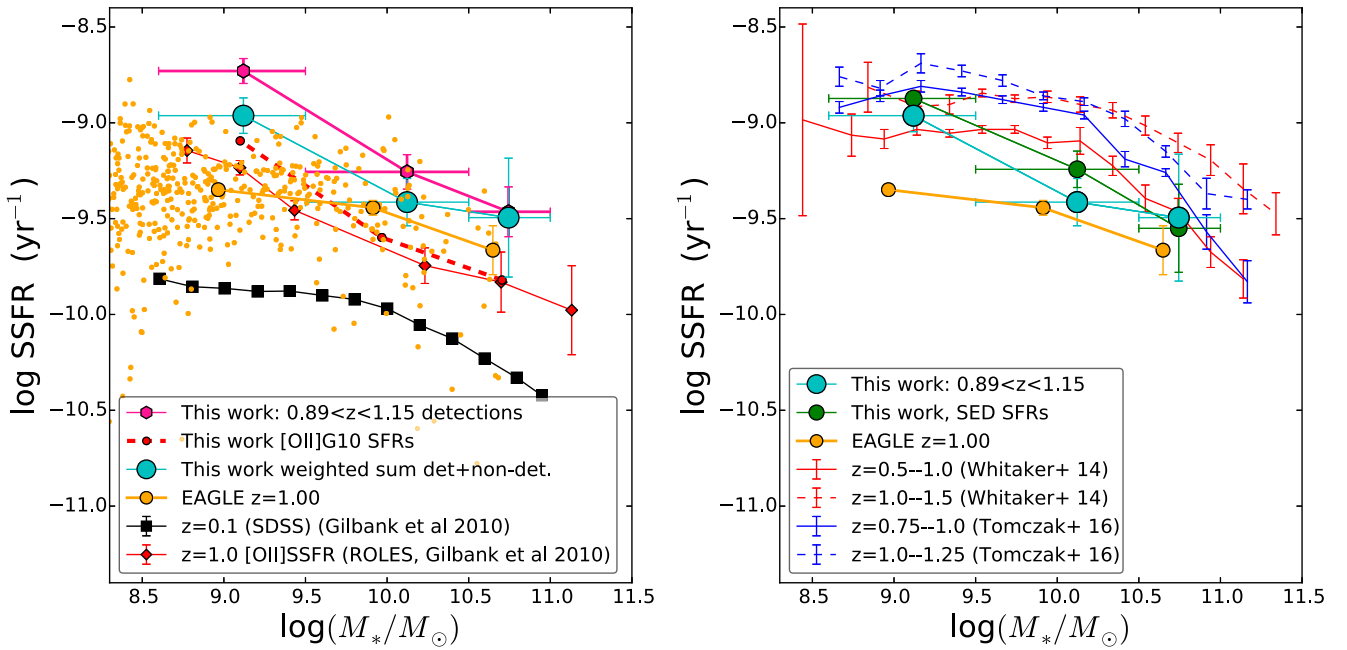


Figure 7. SSFR–mass relation where the SSFR has been measured with $H\alpha$ for this work at $z \sim 1$ (symbols as for previous figure); $[O II]$ from G10 (red circles); and $H\alpha$ from stripe 82 at $z \sim 0.1$ (left-hand panel). Results from the EAGLE simulation RECAL-L025N0752 are shown as orange points, with the median shown as larger connected circles. In addition, the right-hand panel shows results from two recent photometric works. Refer to the text for discussion.

The flatter slope measured with our deeper data has important consequences since, as we discuss below, the flatter relation implies a more uniform average star formation history for galaxies of low and intermediate mass.

One additional point that merits comment is the offset between the ROLES $[O II]$ relation and the $H\alpha$ relation measured in this work. This work uses a subset (from GOODS-S) of the galaxies used in the Gilbank et al. (2010a) $[O II]$ result. In order to compare directly, the dashed line in Fig. 7 uses the same $[O II]$ measurements for exactly the same galaxies used in the $H\alpha$ weighted sum (our preferred method, large cyan circles). It can be seen that this lies intermediate between the Gilbank et al. 2010a $[O II]$ result and the current $H\alpha$ result. We showed in Section 4.3 that the two indicators agree on average, when measured for $H\alpha$ detections (i.e. the subset of galaxies represented by the magenta hexagons in Fig. 7). However, it is perhaps not too surprising that the ratio of $H\alpha/[O II]$ might be slightly higher than the measured value (\sim unity) if lower $H\alpha$ SFRs (non-detections) are omitted. It must be remembered that the error bars do not include the uncertainty/scatter in the transformation from $[O II]$ to $H\alpha$. Thus, it is reassuring that the apparent systematic offset between the $[O II]$ SFRs for all the ROLES WFC3 galaxies (dashed) line lies only ≈ 0.1 dex between both the Gilbank et al. 2010a $[O II]$ SSFR–mass relation, and our current $H\alpha$ relation. A thorough investigation of this point will require deeper spectroscopy.

A final note is that the absolute calibration of $H\alpha$ SFR is dependent on the K98 calibration that is likely uncertain at the 0.2 dex level. The independent calibration of Chang et al. (2015) would lower the normalization of the observed measurements by 0.2 dex.

5.1 Comparison with the EAGLE simulations

In order to place our results in a theoretical context, we compare to the Evolution and Assembly of GaLaxies and their Environ-

ments (EAGLE) simulations. The simulations follow the formation of galaxies (and black holes) in a cosmologically representative (100 Mpc^3) volume (Crain et al. 2015; Schaye et al. 2015). The simulations use advanced smoothed particle hydrodynamics (SPH) and state-of-the-art subgrid models to capture the unresolved physics and include reionization, cooling, metal enrichment and energy input from stellar feedback. Black hole growth and feedback from active galactic nuclei are also included. A complete description of the code and physical parameters used can be found in Schaye et al. (2015) and Crain et al. (2015). These simulations have reproduced many of the observed properties of the Universe with unprecedented fidelity (for example, the evolution of the stellar mass function, the evolution of specific SFRs; see Furlong et al. 2015), providing a powerful tool to study galaxy formation and evolution (Lagos et al. 2015; Rahmati et al. 2015; Schaller et al. 2015; Schaye et al. 2015; Trayford et al. 2015). The evolution of the cosmic star formation history was not used to directly set parameters for the model. The models were calibrated to yield the $z = 0.1$ galaxy stellar mass function and central black hole masses as a function of galaxy stellar mass. The prediction of a reasonable cosmic SFH appears to be a consequence of reproducing the observed sizes of present-day galaxies (as well as the local galaxy stellar mass function). As shown in Crain et al. (2015), simulations that reproduce the observed sizes also match the observed star formation history of the Universe well. The star formation histories of galaxies are extensively discussed in Furlong et al. (2015), and we use this as the basis for comparison with our observational measurements. We use the halo and galaxy catalogues available in the EAGLE data base at <http://www.eaglesim.org/database.php> (McAlpine et al. 2016), and focus on galaxies in the Recal-L025N0752 calculation. The particle mass of this calculation is $2.26 \times 10^5 M_\odot$ for gas particles and $1.21 \times 10^6 M_\odot$ for dark matter particles. The particle mass is a factor of 8 smaller than that of the larger volume Ref-L100N1504 calculation, allowing us to study the star formation histories of galaxies as small as $10^8 M_\odot$ in stellar mass.

In Fig. 7, we show the simulated galaxies as orange points, with the average SSFR–stellar mass in the simulation shown as an orange line. Error bars denote the scatter on the mean. Again, our main result from the stacking analysis is shown in cyan. At low masses, the simulation predicts a relation that is almost flat below a mass of $10^{10.5}$. Since the SSFR can be interpreted as the inverse of the galaxy formation time-scale, a flat distribution of specific SFRs implies that galaxies of all stellar masses have similar star formation histories. This is a natural outcome of the simulations, since dark matter haloes have similar growth rates regardless of stellar mass (Fakhouri, Ma & Boylan-Kolchin 2010; Correa et al. 2015). The flatness of relation is therefore a generic feature of galaxy formation models (Bower et al. 2012): relations that rise or decline strongly with stellar mass require indicate that an additional physical scale is involved in galaxy formation. Such a scale is indeed seen in the SSFR of more massive galaxies as star formation is strongly suppressed by feedback from black hole growth in galaxies more massive than $10^{10.5} M_{\odot}$ (Bower et al. 2006; Croton et al. 2006; Dubois et al. 2015, Bower et al. 2017). The normalization of the SSFR–stellar mass relation reflects the steepness of the stellar-mass–halo-mass relation of galaxies and its evolution (Behroozi, Conroy & Wechsler 2010; Moster et al. 2010).

In low-mass galaxies in EAGLE, star formation is regulated by outflows from supernova feedback (implemented by stochastically heating particles in the vicinity of newly formed stars). The mass loading of the outflow is larger in smaller galaxies, because of the binding energy of the halo, which leads to the relatively flat faint-end slope of the galaxy mass function (Crain et al. 2015, Bower et al. 2017).

Comparison between the observed results and the average SSFR–mass relation derived from the stacking analysis demonstrate the critical importance of accounting for selection effects. Without accounting for the upper limits, the data would naively suggest a steeply rising SSFR at lower masses. Such a result would be in stark contrast to the simulation results and would imply the existence of an additional physical process that is not modelled in the EAGLE simulation. However, the $H\alpha$ emission of most low-mass galaxies is not detectable, and such upper limits must be carefully taken into account. Through our stacking analysis, we are able to better estimate the average specific SFR as a function of stellar mass and the average SSFRs of low-mass galaxies drop considerably, bringing the observations more closely in line with the simulation predictions. However, although we measure a significantly flatter low-mass slope than other works, our result is still significantly steeper than that predicted by EAGLE ($\alpha = -0.14 \pm 0.05$, c.f. Table 3).

Fig. 7 also shows the SSFR–mass relation for local galaxies, determined from SDSS Stripe 82 $H\alpha$ data (G10), together with results from the EAGLE simulations. At low redshift, the simulations and observations agree well (see Furlong et al. 2015 for discussion of the differences between the higher resolution Recal-L025N0752, shown here, and the reference simulation Ref-L100N1504). It is a remarkable success of the simulation that the rate of evolution of the relation is so well described, showing that the simulation correctly captures the decline in the cosmic SFRs of galaxies that results from the slowing accretion of dark matter haloes at the present day. In order to strengthen our results, deeper $H\alpha$ spectroscopy aimed at detecting individually the lowest mass objects would both allow us to measure the intrinsic scatter in the SSFR–mass relation, and confirm whether or not our current sample still shows some residual incompleteness, implying at an even flatter low-mass slope.

5.2 Comparison with photometric studies

The majority of work on the low-mass end of the SSFR–mass relation has used photometric information, due to the difficulty in obtaining spectroscopy of sufficient depth. The obvious disadvantages of using only photometry are the potential inaccuracy of photometric redshifts, particularly given the faint magnitudes necessarily associated with these low-mass objects; the systematic differences between SFR indicators using photometric techniques, particularly their sensitivity to longer time-scales than that probed by $H\alpha$ (see e.g. fig. 3 of Gilbank et al. 2010a); and the degeneracy between these two (the covariance between redshift and SFR is rarely properly accounted for in these fits). However, they obviously allow much larger samples to be constructed and it is instructive to compare a couple of recent results with our spectroscopy and with each other. Fig. 7 (right-hand panel) shows the ROLES and EAGLE data together with results from Whitaker et al. (2014) and Tomczak et al. (2016).⁶ In each case, two redshift bins contain the ROLES redshift range, so the two closest bins are shown for each sample. In both cases, there is good agreement between our measurements in our lowest and highest mass bins; however, our intermediate mass bin ($\log(M_*/M_{\odot}) \sim 10$) is lower than both other surveys. This leads to a steeper slope in our data than either of the others. Interestingly, both surveys show good agreement in overall normalization at the low-mass end (where the statistics should be best), with the Tomczak et al. (2016) result being marginally higher. All these works show higher overall normalization at the low-mass end than the EAGLE prediction. To see if these differences could be due to the SFR indicator used, we recalculate the median SSFR–mass relation using our SED-fitted SFRs, fitted at the $H\alpha$ spectroscopic redshift (or $[O II]$ where $H\alpha$ was undetected). This gives the green line shown in Fig. 7. All of our points agree with our $H\alpha$ measurements, within the uncertainties, but the intermediate mass bin has moved upwards to be more consistent with the other photometric SSFR–mass relations. This hints that the differences between studies may, at least partly, be due to the different SFR indicators used. However, although the most discrepant data point is now closer to the other works, this leads to a formally marginally steeper slope ($\alpha = -0.37 \pm 0.04$). Aside from differences in techniques (spectroscopic versus photometric measurements), another important consideration is cosmic variance. Although our field has some overlap with these other works, this is actually a small fraction of the individual photometric samples. Whitaker et al. (2014) covers a total area of 900 arcmin² from several fields in CANDELS, Tomczak et al. (2016) covers a total area of ≈ 400 arcmin². In comparison, our total surveyed area in $H\alpha$ is ≈ 100 arcmin² in GOODS-S. Our redshift range covered is comparable to the bin sizes used in Tomczak et al. (2016) $0.89 < z \leq 1.15$. So, the ratio in volumes is approximately the ratio in survey area. See Tomczak et al. (2016) for some discussion of the likely impact of cosmic variance on these works. Given the agreement with our higher and lower mass bins, it is unlikely that cosmic variance is responsible for the difference in intermediate masses and more likely reflects a real difference in slope between the measurements. Resolving this will again require larger deep spectroscopic samples.

⁶ We use their ‘SFRsf’ sample as being closest to our selection. Using ‘SFRall’ lowers the SSFR marginally (by including lower SSFR systems), but still within the intrastudy difference.

6 CONCLUSIONS

We have studied a sample of low-mass galaxies ($M_* \sim 10^{8.5} M_\odot$) taken from the ROLES survey at $z \sim 1$ with the aim of determining their SFRs using a more direct SFR indicator, $H\alpha$. These systems were analysed using NIR slitless spectroscopic data from *HST*. We measured the $H\alpha$ emission line luminosities and converted these into SFRs.

(i) We have shown, by comparison of our SED-inferred dust extinction with Balmer decrement corrected SFRs, that the Calzetti relation for estimating gas phase extinction ($A_{\text{gas}} = 2.27A_{\text{stars}}$) overestimates the extinction in $H\alpha$ in line with other recent works. We adopt a fiducial relation of $A_{\text{gas}} = 1.0 A_{\text{stars}}$ as a lower limit to the SFR throughout but discuss alternative choices motivated by other recent results.

(ii) In this study, we compare our $H\alpha$ SFRs with the $[\text{O II}]$ SFRs from ROLES. We find that the ratio of the $H\alpha$ and $[\text{O II}]$ SFRs is consistent, within the broad uncertainties, with the $[\text{O II}]/\text{G10}$ mass-dependent empirical relation calibrated at $z \sim 0.1$. The fact that these two SFRs are comparable implies that the technique for measuring SFRs using ground-based spectroscopy, which is currently more efficient than obtaining $H\alpha$ SFRs from space, is accurate.

(iii) We measure a flatter low-mass power-law slope (-0.47 ± 0.04) to the $z \sim 1$ SSFR–mass relation than found by other (shallower) $H\alpha$ -selected samples (≈ -1), although still somewhat steeper than that predicted by the EAGLE simulation (-0.14 ± 0.05), hinting at possible missing physics not modelled by EAGLE or remaining incompleteness for our $H\alpha$ data.

Deeper *HST* slitless spectroscopy would allow us to attempt to directly detect the $H\alpha$ emitters contributing to our stack, confirming these stacking results and enabling a measurement of the intrinsic scatter in the SSFR–mass relation in this critical low-mass regime. These data would also provide a more direct estimate of completeness, addressing whether there is room in the observational results for an even flatter low-mass slope.

ACKNOWLEDGEMENTS

We thank the anonymous referee for useful comments that improved this work. We thank Tom Jarrett and Andrew Hopkins for comments on an earlier form of this work, as RR's MSc thesis. This work is based on observations taken by the 3D-HST Treasury Program (GO 12177 and 12328) with the NASA/ESA *HST*, which is operated by the Association of Universities for Research in Astronomy, Inc., under NASA contract NAS5-26555. RR, DGG, SLB and RES acknowledge financial support from the National Research Foundation (NRF) of South Africa, RR additionally acknowledges support from the National Astrophysics and Space Science Programme (NASSP) and the University of Cape Town. MLB would like to acknowledge support from an NSERC Discovery grant. RGB acknowledges the support of STFC consolidated grant ST/L00075X/1.

The data used in this paper may be obtained on request from the corresponding author.

REFERENCES

Atek H. et al., 2010, *ApJ*, 723, 104
 Baldry I. K., Glazebrook K., Brinkmann J., Ivezić Ž., Lupton R. H., Nichol R. C., Szalay A. S., 2004, *ApJ*, 600, 681

Balogh M. L., Baldry I. K., Nichol R., Miller C., Bower R., Glazebrook K., 2004, *ApJ*, 615, L101
 Balogh M. L. et al., 2011, *MNRAS*, 412, 2303
 Bayliss K. D., McMahon R. G., Venemans B. P., Ryan-Weber E. V., Lewis J. R., 2011, *MNRAS*, 413, 2883
 Behroozi P. S., Conroy C., Wechsler R. H., 2010, *ApJ*, 717, 379
 Bertin E., Arnouts S., 1996, *A&AS*, 117, 393
 Bower R. G., Benson A. J., Malbon R., Helly J. C., Frenk C. S., Baugh C. M., Cole S., Lacey C. G., 2006, *MNRAS*, 370, 645
 Bower R. G., Benson A. J., Crain R. A., 2012, *MNRAS*, 422, 2816
 Bower R. G., Schaye J., Frenk C. S., Theuns T., Schaller M., Crain R. A., McAlpine S., 2017, *MNRAS*, 465, 32
 Brammer G. B. et al., 2009, *ApJ*, 706, L173
 Brammer G. B. et al., 2012, *ApJS*, 200, 13
 Buat V. et al., 2005, *ApJ*, 619, L51
 Calzetti D., Armus L., Bohlin R. C., Kinney A. L., Koornneef J., Storchi-Bergmann T., 2000, *ApJ*, 533, 682
 Caputi K. I. et al., 2008, *ApJ*, 680, 939
 Charlot S., Longhetti M., 2001, *MNRAS*, 323, 887
 Chang Y.-Y., van der Wel A., da Cunha E., Rix H.-W., 2015, *ApJS*, 219, 8
 Correa C. A., Wyithe J. S. B., Schaye J., Duffy A. R., 2015, *MNRAS*, 450, 1514
 Crain R. A. et al., 2015, *MNRAS*, 450, 1937
 Croton D. J. et al., 2006, *MNRAS*, 365, 11
 Cucciati O. et al., 2012, *A&A*, 539, A31
 Dale D. A. et al., 2010, *ApJ*, 712, L189
 Davies G. T. et al., 2009, *MNRAS*, 395, L76
 Dubois Y., Volonteri M., Silk J., Devriendt J., Slyz A., Teyssier R., 2015, *MNRAS*, 452, 1502
 Erb D. K., Shapley A. E., Pettini M., Steidel C. C., Reddy N. A., Adelberger K. L., 2006, *ApJ*, 644, 813
 Faber S. M. et al., 2007, *ApJ*, 665, 265
 Fakhouri O., Ma C.-P., Boylan-Kolchin M., 2010, *MNRAS*, 406, 2267
 Fioc M., Rocca-Volmerange B., 1997, *A&A*, 326, 950
 Fumagalli M. et al., 2012, *ApJ*, 757, L22
 Furlong M. et al., 2015, *MNRAS*, 450, 4486
 Garn T., Best P. N., 2010, *MNRAS*, 409, 421
 Geach J. E., Smail I., Best P. N., Kurk J., Casali M., Ivison R. J., Coppin K., 2008, *MNRAS*, 388, 1473
 Gilbank D. G. et al., 2010a, *MNRAS*, 405, 2419
 Gilbank D. G., Baldry I. K., Balogh M. L., Glazebrook K., Bower R. G., 2010b, *MNRAS*, 405, 2594 (G10)
 Glazebrook K., Blake C., Economou F., Lilly S., Colless M., 1999, *MNRAS*, 306, 843
 Glazebrook K. et al., 2004, *Nature*, 430, 181
 Henriques B. M. B., White S. D. M., Thomas P. A., Angulo R. E., Guo Q., Lemson G., Springel V., 2013, *MNRAS*, 431, 3373
 Hogg D. W., 1999, preprint ([arXiv:astro-ph/9905116](https://arxiv.org/abs/astro-ph/9905116))
 Hopkins A. M., Beacom J. F., 2006, *ApJ*, 651, 142
 Hopkins A. M., Connolly A. J., Haarsma D. B., Cram L. E., 2001, *AJ*, 122, 288
 Juneau S. et al., 2005, *ApJ*, 619, L135
 Karim A. et al., 2011, *ApJ*, 730, 61
 Kashino D. et al., 2013, *ApJ*, 777, L8
 Kennicutt R. C., Jr 1992, *ApJ*, 388, 310
 Kennicutt R. C., Jr, 1998, *ARA&A*, 36, 189 (K98)
 Kennicutt R. C., Jr, Kent S. M., 1983, *AJ*, 88, 1094
 Kewley L. J., Geller M. J., Jansen R. A., 2004, *AJ*, 127, 2002
 Koekemoer A. M., Fruchter A. S., Hook R. N., Hack W., Hanley C., 2006, in Koekemoer A. M., Goudfrooij P., Dressel L. L., eds, *The 2005 HST Calibration Workshop: Hubble After the Transition to Two-Gyro Mode*. p. 423
 Kroupa P., 2001, *MNRAS*, 322, 231
 Kümmel M., Walsh J. R., Pirzkal N., Kuntschner H., Pasquali A., 2009, *PASP*, 121, 59
 Lagos C. d. P. et al., 2015, *MNRAS*, 452, 3815
 Leja J., van Dokkum P. G., Franx M., Whitaker K. E., 2015, *ApJ*, 798, 115

Lilly S. J., Le Fevre O., Hammer F., Crampton D., 1996, *ApJ*, 460, L1
 Ly C. et al., 2007, *ApJ*, 657, 738
 McAlpine S. et al., 2016, *Astron. Comput.*, 15, 72
 McCarthy P. J. et al., 1999, *ApJ*, 520, 548
 Madau P., Dickinson M., 2014, *ARA&A*, 52, 415
 Madau P., Ferguson H. C., Dickinson M. E., Giavalisco M., Steidel C. C., Fruchter A., 1996, *MNRAS*, 283, 1388
 Mok A. et al., 2013, *MNRAS*, 431, 1090
 Momcheva I. G., Lee J. C., Ly C., Salim S., Dale D. A., Ouchi M., Finn R., Ono Y., 2013, *AJ*, 145, 47
 Momcheva I. G. et al., 2016, *ApJS*, 225, 27
 Mostek N., Coil A. L., Moustakas J., Salim S., Weiner B. J., 2012, *ApJ*, 746, 124
 Moster B. P., Somerville R. S., Maubetsch C., van den Bosch F. C., Macciò A. V., Naab T., Oser L., 2010, *ApJ*, 710, 903
 Noeske K. G. et al., 2007, *ApJ*, 660, L43
 Pérez-González P. G., Zamorano J., Gallego J., Aragón-Salamanca A., Gil de Paz A., 2003, *ApJ*, 591, 827
 Price S. H. et al., 2014, *ApJ*, 788, 86
 Rahmati A., Schaye J., Bower R. G., Crain R. A., Furlong M., Schaller M., Theuns T., 2015, *MNRAS*, 452, 2034
 Reddy N. A. et al., 2015, *ApJ*, 806, 259
 Savaglio S. et al., 2005, *ApJ*, 635, 260
 Schaller M., Dalla Vecchia C., Schaye J., Bower R. G., Theuns T., Crain R. A., Furlong M., McCarthy I. G., 2015, *MNRAS*, 454, 2277
 Schaye J. et al., 2015, *MNRAS*, 446, 521
 Schmitt H. R., Calzetti D., Armus L., Giavalisco M., Heckman T. M., Kennicutt R. C., Jr, Leitherer C., Meurer G. R., 2006, *ApJ*, 643, 173
 Shim H., Colbert J., Teplitz H., Henry A., Malkan M., McCarthy P., Yan L., 2009, *ApJ*, 696, 785
 Skelton R. E. et al., 2014, *ApJS*, 214, 24
 Sobral D., Best P. N., Smail I., Geach J. E., Cirasuolo M., Garn T., Dalton G. B., 2011, *MNRAS*, 411, 675
 Sobral D., Best P. N., Matsuda Y., Smail I., Geach J. E., Cirasuolo M., 2012, *MNRAS*, 420, 1926
 Sobral D., Smail I., Best P. N., Geach J. E., Matsuda Y., Stott J. P., Cirasuolo M., Kurk J., 2013, *MNRAS*, 428, 1128
 Sobral D. et al., 2009, *MNRAS*, 398, 68
 Springel V., Frenk C. S., White S. D. M., 2006, *Nature*, 440, 1137
 Steidel C. C. et al., 2014, *ApJ*, 795, 165
 Tomczak A. R. et al., 2016, *ApJ*, 817, 118
 Trayford J. W. et al., 2015, *MNRAS*, 452, 2879
 Tresse L., Maddox S. J., Le Fèvre O., Cuby J.-G., 2002, *MNRAS*, 337, 369
 Twite J. W., Conselice C. J., Buitrago F., Noeske K., Weiner B. J., Acosta-Pulido J. A., Bauer A. E., 2012, *MNRAS*, 420, 1061
 van Dokkum P. G. et al., 2011, *ApJ*, 743, L15
 Vanzella E. et al., 2008, *A&A*, 478, 83
 Villar V., Gallego J., Pérez-González P. G., Pascual S., Noeske K., Koo D. C., Barro G., Zamorano J., 2008, *ApJ*, 677, 169
 Whitaker K. E., van Dokkum P. G., Brammer G., Franx M., 2012, *ApJ*, 754, L29
 Whitaker K. E. et al., 2014, *ApJ*, 795, 104
 White S. D. M., Frenk C. S., 1991, *ApJ*, 379, 52
 White S. D. M., Rees M. J., 1978, *MNRAS*, 183, 341
 Willmer C. N. A. et al., 2006, *ApJ*, 647, 853
 Wuyts S. et al., 2013, *ApJ*, 779, 135
 Zhu G., Moustakas J., Blanton M. R., 2009, *ApJ*, 701, 86

APPENDIX A: FLUX REPEATABILITY TEST

In our sample, there are galaxies that have multiple spectra from repeated *HST* observations in overlapping fields. These spectra are used to test the repeatability of our flux measurements, the $(S/N)_{\text{peak}}$ and wavelength accuracy.

Originally, the spectrum with the lowest σ was chosen for our catalogue (as is commonly done when combining catalogues). We show why this leads to a bias in the $H\alpha$ measurements, and our alternate approach to negate this bias.

The repeatability of our flux measurements was tested by comparing the ratio of the observed errors to the expected errors for each. This ratio was computed as follows;

$$\frac{F(H\alpha)_{\text{used}} - F(H\alpha)_{\text{rep}}}{\sqrt{\sigma_{\text{used}}^2 + \sigma_{\text{rep}}^2}}, \quad (\text{A1})$$

where $F(H\alpha)_{\text{used}} - F(H\alpha)_{\text{rep}}$ is the observed error obtained from the difference between the line flux used in the catalogue ($F(H\alpha)_{\text{used}}$) and the flux from repeat observations ($F(H\alpha)_{\text{rep}}$). The expected error is the sum in quadrature of the errors on the flux measurement used in the catalogue (σ_{used}) and from repeat observations (σ_{rep}). If these errors have been calculated properly, a normal distribution, with a mean of zero, is expected. It was found that there is an offset in the mean ($\mu \sim 1.5$). This offset is because we initially chose the lowest σ spectrum to use in the catalogue that creates a bias. We corrected this bias by replacing the lowest σ spectrum for a galaxy with multiple spectra with another randomly selected spectra to use in the catalogue. This reduces the mean offset to 0.68. In addition, calculating the dispersion of this second sample gives $\sigma = 1.0$, showing that our flux uncertainties are repeatable.

APPENDIX B: S/N REPEATABILITY

In Section 3, we chose a detection threshold of 5σ ($S/N \geq 5$) based on visually inspecting spectra where there were obvious bright emission lines. In this section, we test whether this threshold is reasonable and if it really corresponds to a 5σ detection. As mentioned before, choosing a threshold is a trade-off between purity and completeness. We can test our threshold by determining the reproducibility of the emission lines for galaxies that have multiple spectra. Our criteria for whether a detection is real or not is that the line should be found in the majority of the spectra (e.g. if a galaxy has four spectra, the line should be seen in three out of the four spectra) to be considered reproduced. The best way to test this is to pick a spectrum where the line has a very high $(S/N)_{\text{peak}}$ because it is more likely to be a real detection. An example of a galaxy that has four spectra, with a high $(S/N)_{\text{peak}}$, is shown in Fig. B1. A line is seen in all the spectra meaning that the line is reproduced.

In Fig. B2, we plot the S/N used in our catalogue against the S/N from repeat spectra. Moving from right to left (high to low $(S/N)_{\text{peak}}$) in Fig. B2, we look at the points in the vertical direction because these correspond to the same galaxy and check to see if they lie above our chosen threshold. If they do, we count them as recovered. However, the chosen threshold has some uncertainty on it so when deciding if a spectrum is recovered, we also count those points that lie fairly close, within $\delta(S/N)_{\text{peak}} = 0.3$, to the chosen threshold as recovered. We only go down to $(S/N)_{\text{peak}} = 3$ to see how many galaxies we can recover because we do not believe any detections below $(S/N)_{\text{peak}} = 3$. The fraction of recovered galaxies is plotted in Fig. B3. This plot shows that for our sample of galaxies that have repeat spectra, we recover 60–100 per cent of galaxies between $(S/N)_{\text{peak}} = 3$ and 5. Based on Fig. B3, if we look at the $(S/N)_{\text{peak}}$ distribution in our catalogue (see Fig. 3) and apply a

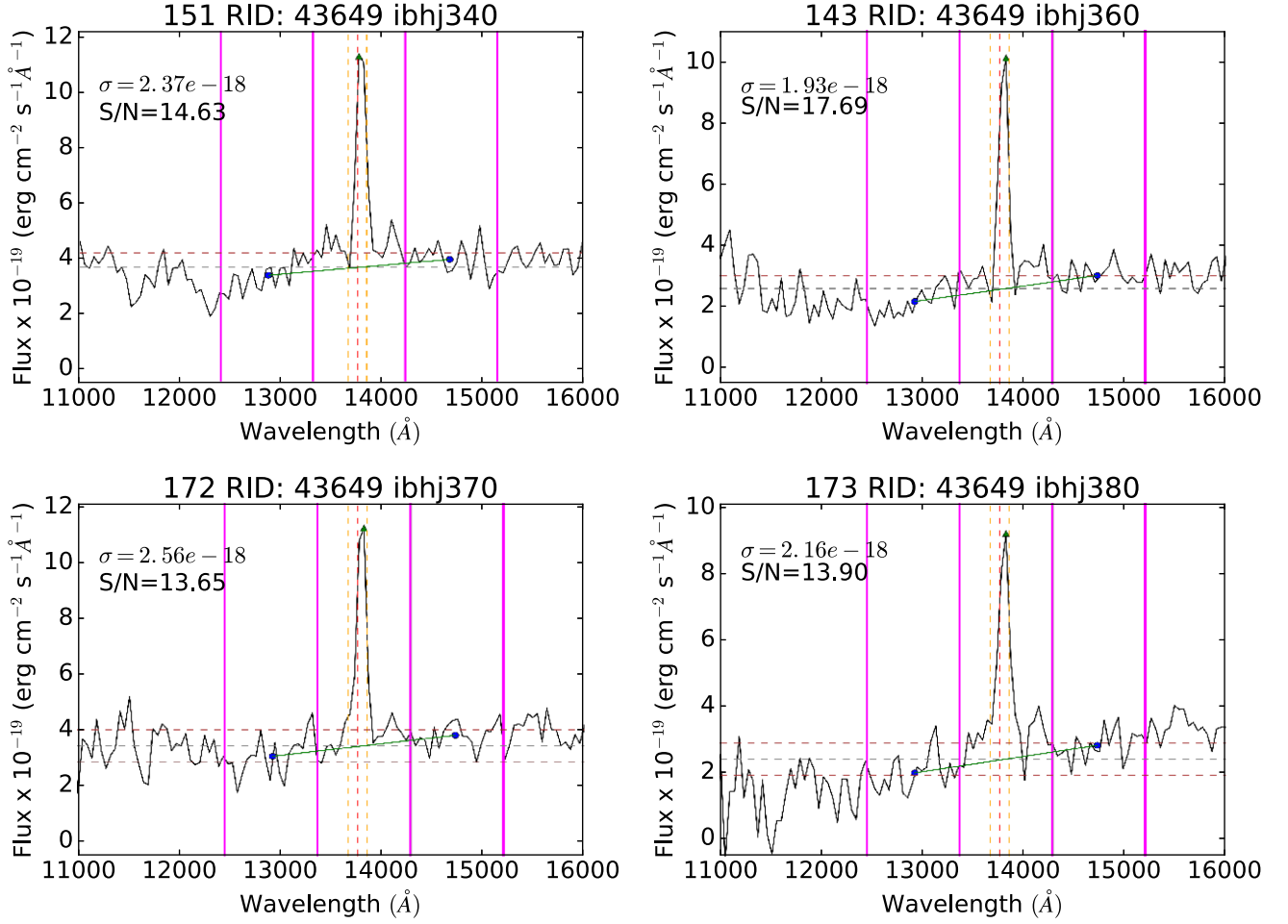


Figure B1. Example of a galaxy's spectrum with a high $(S/N)_{\text{peak}}$ emission line in four pointings. The emission line is seen in all pointings meaning that it is reproduced. Lines and symbols have the same meaning as in Fig. 2.

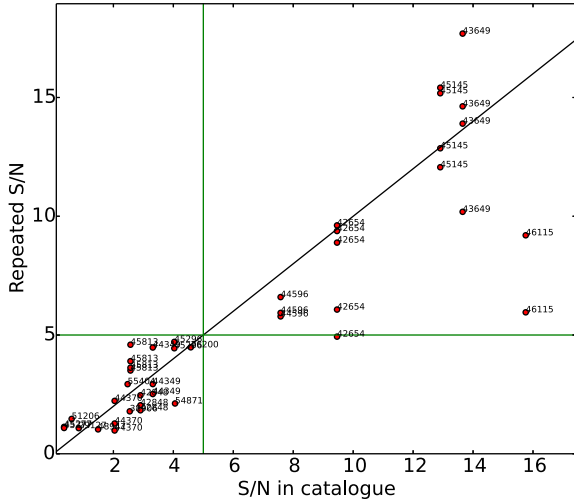


Figure B2. $(S/N)_{\text{peak}}$ from repeat spectra against S/N used in catalogue. Green lines indicate the $(S/N)_{\text{peak}} = 5$ threshold.

$(S/N)_{\text{peak}} = 4.5$ threshold, for example, we get 18 detections out of which 80 per cent are real and 20 per cent are spurious. Our initial threshold of $(S/N)_{\text{peak}} = 5$, thus gives us a pure sample but we are missing some real detections.

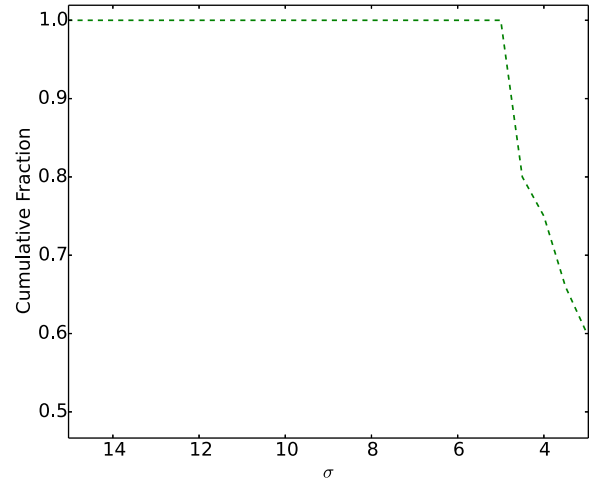


Figure B3. Recovered fraction of galaxies from our sample of galaxies with multiple spectra.

APPENDIX C: COMPARISON WITH 3D-HST

With the recent public release (Momcheva et al. 2016) of 3D-HST reductions and derived products (redshifts, emission line fluxes, etc.) of the spectroscopic data we have used in this work, it is possible to compare their results with the independent measurements made by

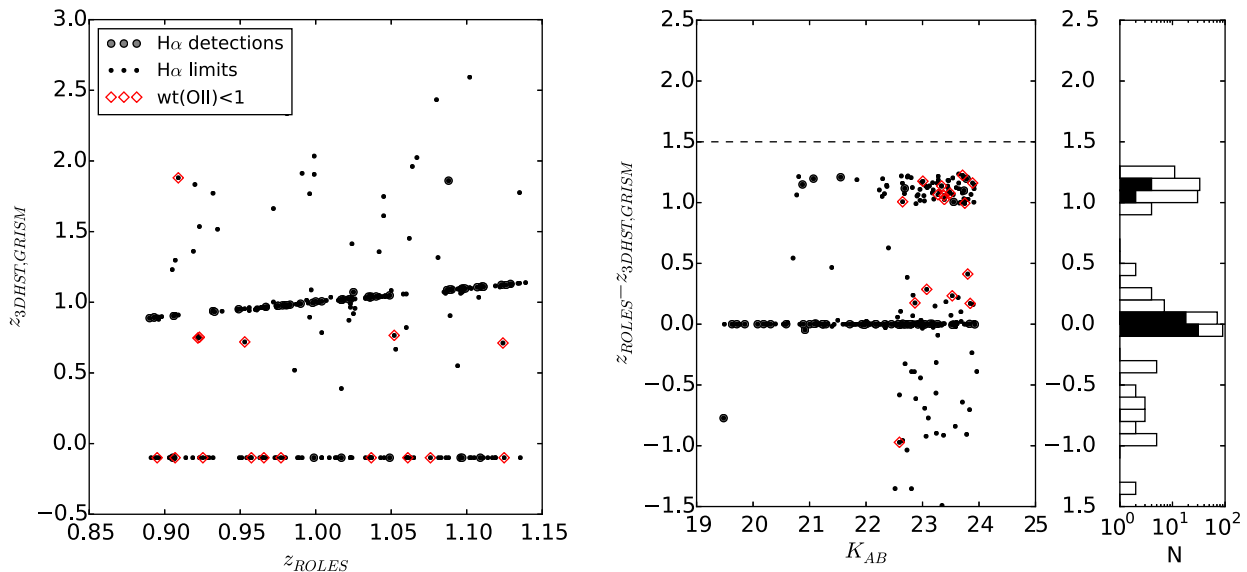


Figure C1. Comparison of our redshifts with 3D-HST. Left-hand panel: our redshifts versus those of 3D-HST. Larger filled symbols denote $\sigma \geq 5$ detections in our data; open red diamonds show lower confidence ROLES redshifts with $wt([OII]) < 1$ (see the text for discussion). Right-hand panel: redshift difference as a function of apparent K -band magnitude. Symbols are same as in the left-hand panel. Objects with no corresponding redshift in 3D-HST are shown at $\Delta z > 1.5$ (and $z < 0$ in left-hand panel). Histograms show the number of objects in the whole sample (open histogram) and those with ROLES $H\alpha$ detections (filled histogram). Note the log scale.

this work. Fig. C1 compares the redshifts of the two works. In the left-hand panel, the two redshifts are plotted against one another, and in the right-hand panel, the redshift difference is shown as a function of apparent K -band magnitude, with a histogram showing the number of objects as a function of the residual. In these plots, objects with a ROLES’ redshift but not a corresponding 3D-HST redshift are plotted at -1.0 on the vertical axis in the left plot and in the region above 1.5 in the vertical axis on the right-hand panel. From these, it is clear that there is overall good agreement where a redshift is measured in both works. Where $H\alpha$ is detected in our analysis, only two out of 50 galaxies show disagreement at the $\Delta z > 0.01$ level (which is $\sim 3\sigma$ level set by the resolution of the grism spectra) with 3D-HST redshifts. Recall that ROLES is based on $[OII]$ detections in deeper optical spectroscopy (in terms of SFR probed at $z \sim 1$). Where an emission line was detected in ROLES, its probability of being $[OII]$ was compared with the probability of being another line using photometric redshift (photo- z) PDFs. This resulted in a probability of being $[OII]$ versus that of being another common line visible in the ROLES’ wavelength window, $wt([OII])$.⁷ For 3D-HST, redshifts are estimated from full spectral fits to the grism spectroscopy, combined with photo- z information from an updated photometric data set (Skelton et al. 2014). So, in principle, 3D-HST redshifts should be more secure than that used by the ROLES parent sample. However, the average ROLES galaxy is a K -faint galaxy with little continuum in the WFC3 grism data, and likely relatively noisy photometry from which to derive a photo- z . Thus, it is not surprising that a significant fraction (7/57 for $H\alpha$

Table C1. Summary of comparison with 3D-HST shown in Fig. C1. See the text for discussion.

Sample	N in sample	N with $\Delta z < 0.01$	N with no 3D-HST $H\alpha$ detection
ROLES $H\alpha$ detections only	57	48	7
ROLES $H\alpha$ detections + limits	281	78	140

detections, and 140/281 in the whole ROLES sample) have no secure grism redshift from 3D-HST. The results of this comparison are tabulated in Table C1.

Fig. C2 shows a comparison with 3D-HST $H\alpha + [NII]$ fluxes (Momcheva et al. 2016). In this comparison, neither catalogue is corrected for the contribution of $[NII]$. Our simple aperture measurement shows reasonable agreement with the sophisticated technique used by Momcheva et al. (2016); however, we see an overall trend that our fluxes lie systematically around 20 per cent fainter. Momcheva et al. (2016) used model fitting of the continuum (compared with our local linear fit) plus a renormalization of the absolute flux based on extensive multiwavelength photometry. So, although we use the same HST spectroscopy (albeit with a different extraction and measurement method), the overall calibration appears systematically different. Shifting our calibration to agree for this would only raise our $H\alpha$ luminosities, and hence SFRs by 0.08 dex.

C1 Completeness

The spectroscopic completeness of the parent ROLES sample used in this work ($[OII]$ -selected) was presented in Gilbank et al. (2010a) (see in particular fig. 12). For the GOODS-S field, it was estimated to be $\gtrsim 80$ per cent independent of magnitude, down to the survey limit of $K = 24.0$. The 3D-HST data allow us to reassess this with the benefit of deeper data and higher precision photo- z s. However, it must be borne in mind that photometric redshifts are not well tested at these faint magnitudes. In Gilbank et al. (2010a), we showed

⁷ See Gilbank et al. (2010a) for more details. Briefly, almost every single emission line detection was more likely to be $[OII]$ than another, lower redshift line. A weighting was calculated based on the ratio of photo- z PDFs and if the ratio was > 0.9 in favour of $[OII]$ it was set to unity. Conversely, if the probability was < 0.1 , its value was set to 0. Everything in between was kept as the formal ratio of probabilities of other redshifts and these measurements received fractional weighting in our analysis.

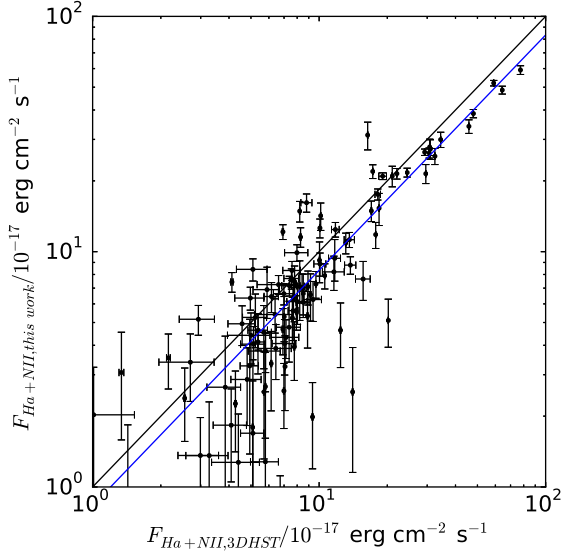


Figure C2. Comparison of our $H\alpha$ + $[NII]$ fluxes with those measured by 3D-*HST*. This shows that our simple aperture measurement compares favourably to the technique used by which attempts a more sophisticated fitting of the continuum, plus a renormalization based on the multiwavelength imaging data available. The black line shows the one-to-one relation. It appears that the 3D-*HST* fluxes are higher than ours by about 20 per cent (indicated by blue line). See text for discussion.

how we targeted almost every galaxy in our K -band magnitude range ($22.5 < K \leq 24.0$, independent of photo- z , and only used the (FIREWORKS) photo- z PDFs to break degeneracies between most likely emission lines at other redshifts outside our target window ($0.89 < z \leq 1.15$). With these caveats in mind, we can proceed to examine the galaxies that 3D-*HST* photometric data places within

our desired stellar mass and redshift ranges and see what fraction we (a) placed slits on, (b) obtained $[OII]$ detections.

Fig. C3 shows the completeness estimated by comparison with 3D-*HST* photometric redshifts. The left-hand panel shows the ROLES-observed targets as a function of K -band magnitude. The magnitudes (and masses) are taken from 3D-*HST* photometry, in order to be consistent with the photometric redshifts used. Several caveats must be noted. Since ROLES used K -band selection ($22.5 < K_{AB} \leq 24.0$), differences between K photometry in 3D-*HST* versus FIREWORKS can lead to objects being lost from this plot. Indeed, at the faintest magnitudes there is significant scatter (~ 0.3 mag). The left-hand panel shows all the slits we placed (where ‘slits’ specifically refers to ROLES slits and does not include the ESO brighter sample, since we do not have the targeting information for that) for all objects (regardless of 3D-*HST* photometric redshift); those within the redshift window (equivalent to spectroscopic/targeting completeness); and those which resulted in an emission line consistent with $[OII]$ (equivalent to redshift success rate). The right-hand panel shows the equivalent as a function of stellar mass. Again, an important caveat is that the stellar masses here all come from 3D-*HST* (except where noted) and so there is some degeneracy between fitting the stellar mass and photometric redshift to the same photometry. Typically the covariance between the parameters is ignored, and the best-fitting photo- z is simply assumed to be correct. In order to assess the possible impact of this, the redshift success rate is shown as a function of stellar mass calculated from our own SED fitting at the spectroscopic redshift, and 3D-*HST*’s stellar masses at their (mostly photometric) redshifts.

The overall targeting completeness is somewhat lower than calculated in Gilbank et al. (2010a) that was approximately 80 per cent independent of stellar mass. This is likely due to a combination of the reasons mentioned above (difference in K -band photometry between 3D-*HST* and FIREWORKS; improved precision of photo- z s, and inclusion of grism redshifts, versus FIREWORKS broader

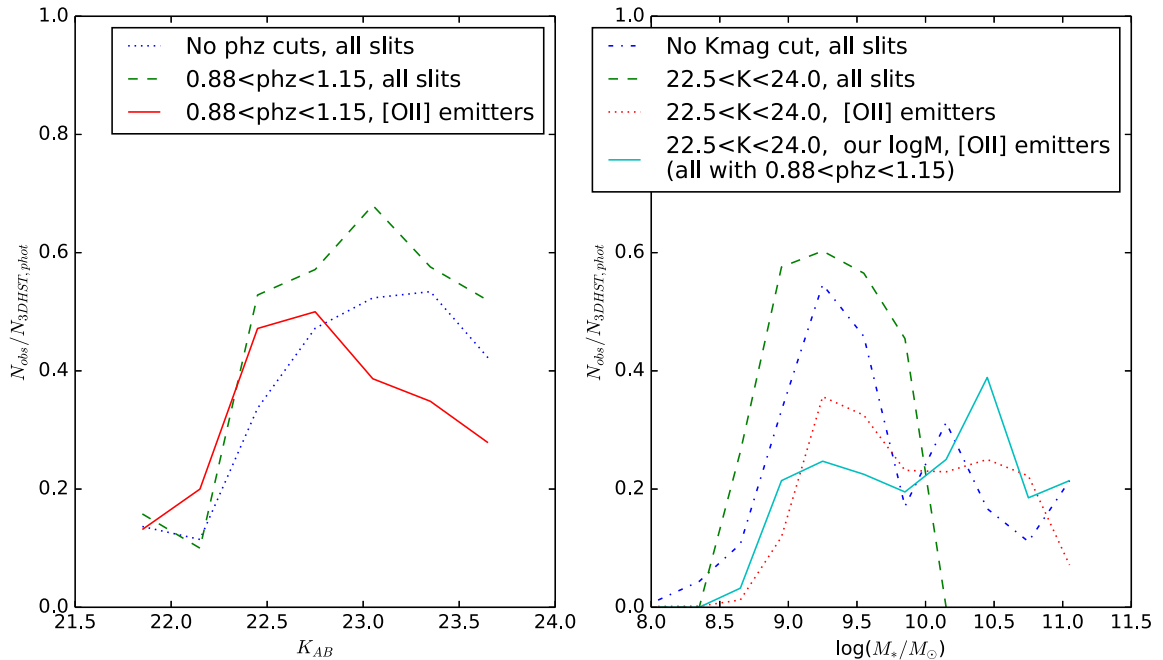


Figure C3. Left-hand panel: test of completeness as a function of apparent K -band magnitude from 3D-*HST* catalogues. Results are shown for all objects regardless of photo- z ; for those with 3D-*HST* photo- z s in our redshift window (‘spectroscopic/targeting completeness’); and for those which resulted in $[OII]$ detections (‘redshift success rate’). Right-hand panel: similar tests as a function of stellar mass. In all cases except solid cyan line, masses come from 3D-*HST*. See the text for discussion.

photo- z PDFs); but also might reflect the limitations of the different photometric redshifts at these faint magnitudes. Indeed, an instructive exercise is to plot independent photometric redshift estimates from different codes from the same data at these faint magnitudes and the scatter is generally surprisingly large (M. Franx, private communication)! So, the completenesses shown in the plot should be regarded as lower limits.

For the higher mass, ESO public spectroscopic sample (Vanzella et al. 2008), pertinent details of the selection were discussed in Gilbank et al. (2010a) and we briefly summarize the salient points here. The survey was z -band selected but otherwise comparable to ROLES in terms of spectroscopic depth, and the 1D spectra were processed for emission line measurements in the same way as for ROLES. Although the follow-up comprised specific sub-samples, such as X-ray selected targets, we rejected the small number of

objects in our redshift window showing both [O II] and X-ray emission (as possible AGN) as well as likely AGN from *Spitzer* colours. Thus, we found the spectroscopic (targeting) completeness to be ~ 40 per cent in each K magnitude bin except for the brightest bin ($K < 22.75$) that is about 70 per cent complete.

Finally, it is worth noting that our highest mass SSFR measurements are in good agreement with literature values, and so our measurements of the slope of the SSFR relation are not limited by uncertainties in the high-mass (ESO public spectroscopic) sample.

This paper has been typeset from a \LaTeX file prepared by the author.